JGR Atmospheres

RESEARCH ARTICLE
10.1029/2021JD035822

Key Points:

- A positive correlation exists between the magnitudes of size sorting signatures and convective depth
- Larger size sorting magnitudes are associated with more riming growth and quicker graupel fallout
- Intense convective precipitation in the PECAN MCSs seems to be dominated more by cold rain processes than warm rain processes

Correspondence to:
M.-J. Yang,
mingjen@as.ntu.edu.tw

Citation:
Tam, F. I.-H., Yang, M.-J., & Lee, W.-C. (2022). Polarimetric size sorting signatures in the convective regions of mesoscale convective systems in PECAN: Implications on kinematics, thermodynamics, and precipitation pathways. *Journal of Geophysical Research: Atmospheres*, *127*, e2021JD035822. https://doi.org/10.1029/2021JD035822

Received 7 SEP 2021
Accepted 25 APR 2022

Author Contributions:
Conceptualization: Ming-Jen Yang
Data curation: Wen-Chau Lee
Formal analysis: Frederick Iat-Hin Tam
Investigation: Frederick Iat-Hin Tam
Methodology: Ming-Jen Yang
Resources: Wen-Chau Lee
Software: Frederick Iat-Hin Tam
Supervision: Ming-Jen Yang
Validation: Frederick Iat-Hin Tam, Wen-Chau Lee
Writing – original draft: Frederick Iat-Hin Tam
Writing – review & editing: Ming-Jen Yang

Polarimetric Size Sorting Signatures in the Convective Regions of Mesoscale Convective Systems in PECAN: Implications on Kinematics, Thermodynamics, and Precipitation Pathways

Frederick Iat-Hin Tam[1], Ming-Jen Yang[1], and Wen-Chau Lee[2]

[1]National Taiwan University, Taipei, Taiwan, [2]National Center for Atmospheric Research, Boulder, CO, USA

Abstract An object-based technique was utilized to identify hydrometeor size-sorting signatures at lower levels in the convective regions of 10 mesoscale convective systems (MCSs) during the 2015 Plains Elevated Convection at Night (PECAN) field campaign. Composite statistical analysis indicates that the magnitudes of size-sorting signatures (the separation distances between rain diameter maxima and concentration maxima) are nonlinearly correlated to the echo-top height, rain mass beneath the melting level, and precipitation rates at higher percentiles. To explore this correlation, the weather forecasting and research model was used to simulate the 20 June 2015 MCS during PECAN. Statistical analysis of the model outputs indicates more active riming growth and quicker graupel fallout at warmer temperatures near areas with larger separation distances. While updraft intensity above the melting level was also positively correlated to separation distances, this correlation was only statistically significant within certain temperature ranges. Additional analyses reveal that the higher intense precipitation potential near signatures with large separation distances could be attributed to precipitation production from the melted graupel. Finally, spatial correspondence between graupel distribution at the melting level and rain distribution at the lowest model level illustrates the critical role of graupel sedimentation and sorting in creating size-sorting signatures in MCSs during the PECAN field experiment.

Plain Language Summary Recent upgrades in the US radar networks to polarimetric capabilities enabled routine measurements of how the sizes and concentration of raindrops vary in weather systems. Statistical analysis of radar data and output from a numerical model shows that the spatial distributions of raindrop sizes and concentration in the low levels could be exploited to elucidate physical processes in rainy weather systems. Specifically, low-level raindrop size-concentration separation may provide extra information on how much latent heating is released or absorbed when water transitions between vapor, liquid, and solid phases. This new information could be important because heating aloft can affect the intensity of the weather systems and the amount of precipitation produced by weather systems.

1. Introduction

Understanding the microphysical processes of organized mesoscale convective systems (MCSs) and accurately parameterizing them in numerical models remains a great challenge for weather forecasters and scientists. One of the factors limiting the improvement in the prediction of storm microphysics is the lack of three-dimensional observations on the drop size distributions (DSDs) of hydrometeors within the MCSs. Biases in the DSDs have substantial impacts on model performance. Idealized numerical simulations have shown that prescribed raindrop DSDs and the treatment of raindrop breakup and size sorting yield substantial influences on the MCS characteristics like cold-pool intensity and low-level lifting through raindrop evaporation (Dawson et al., 2010; Morrison et al., 2012; Planche et al., 2019). In practice, we mostly rely on research flights and disdrometers to acquire *in-situ* measurements of hydrometeor DSDs. However, airborne measurements are costly, and only limited observation data can be collected during field campaigns. An advantage of airborne platforms is that they directly captured the DSD characteristics within the storm and how DSD varies with altitude (e.g., Stechman, McFarquhar, Rauber, Bell, et al., 2020) during flight hours. Ground-based disdrometers cannot provide DSD information in the vertical but can provide *surface* DSD measurements over a longer period of time.

Polarimetric radars provide an alternative method to estimate the three-dimensional DSD information in weather systems with greater spatial details and higher temporal frequency. Among various polarimetric variables, differential reflectivity (Z_{DR}) and specific differential propagation phase (K_{DP}) are particularly useful in characterizing DSDs. The Z_{DR} is the ratio between reflectivity factors in the horizontal and vertical polarization. The Z_{DR} reveals

the dominant particle shape within a radar sampling volume, with $Z_{DR} > 0$ dB indicating the volume to be dominated by oblate particles. The K_{DP} measures the range-dependent phase changes of the horizontally- and vertically-polarized radar waves. Positive K_{DP} are expected in areas with (a) a high concentration of oblate rain drops, (b) small melting hailstones, and (c) aggregates of oblate ice crystals (Rauber & Nesbitt, 2018).

The use of polarimetric radars for severe weather systems has revealed DSD signatures that were unobserved previously. These signatures include the enhanced Z_{DR} along reflectivity gradients in the forward flanks of supercells (Z_{DR} arcs; Dawson et al., 2014; Kumjian & Ryzhkov, 2008), and the Z_{DR}-K_{DP} separations in different shear quadrants of hurricane eyewalls (Didlake & Kumjian, 2018; Feng & Bell, 2018; Laurencin et al., 2020). Since hydrometeor fall speeds are positively correlated to particle sizes, larger particles should sediment quicker and experience less wind advection (large Z_{DR}) than the remaining smaller particles (large K_{DP}). This process, known as hydrometeor size sorting, could result in the observed Z_{DR}-K_{DP} separations.

While observational studies of hydrometeor size sorting are plentiful in the literature, further investigation is still needed to clarify the uncertainties in this process. The first uncertainty is how the size sorting of ice hydrometeors contributes to the variabilities of low-level rain DSD. Dawson et al. (2015) (hereafter DMR15) showed that inputting supercell hodographs to a rain sedimentation model was sufficient in producing the low-level DSD variabilities which were similar to the Z_{DR} arcs. Similarly, Laurencin et al. (2020) (hereafter LDL20) reported that applying the low-level winds of Hurricane Matthew in 2016 to an analytical model recreated the Z_{DR}-K_{DP} azimuthal separation in Matthew's eyewall. However, DMR15 and LDL20 restricted their investigation to the sorting of rain shafts with prescribed DSDs and did not consider ice sorting aloft. Indeed, numerical simulations with free-evolving DSDs of ice particles indicated that deep-layer storm-relative winds and the sorting of hail particles are more important than the sorting of raindrops in producing the Z_{DR} arcs in the left flank of right-moving supercells (Dawson et al., 2014). The second uncertainty is the role of updrafts. While both updrafts and storm-relative winds can lead to sustained size sorting (Kumjian & Ryzhkov, 2012), previous studies (e.g., DMR15; LDL20; Loeffler et al., 2020) mostly focused on storm-relative winds. These studies implicitly assumed that the effect of storm-relative winds overwhelmed that of the updrafts. This assumption is reasonable for supercells and tropical cyclones (TCs), which have intense horizontal cyclonic flows. While Feng and Bell (2018) also considered how TC updrafts and downdrafts may affect DSD distributions, the link between updrafts and low-level DSD spatial distributions in other weather systems remains an open question. For example, updrafts may be more important in regulating the size-sorting signatures in squall-line MCSs, where the circulations are more two-dimensional than those in supercells.

In addition to addressing the above uncertainties, we are also interested to know whether or not the magnitudes of Z_{DR}-K_{DP} separations (size-sorting magnitudes) can be used to evaluate convective variabilities. Yuter and Houze (1995b) suggested that hydrometeor trajectories in MCSs could be understood by the "particle fountain" model. Larger hydrometeors formed in updraft core sediment closer to the updrafts due to gravity sorting, whereas smaller hydrometeors sediment further rearward as updraft cores expanded and advected rearward by the front-to-rear flow. Based on the "particle fountain" model, we hypothesize that larger size-sorting magnitudes would positively correlate to ice growth, rearward advection of smaller ice hydrometeors, and updraft intensity.

In this study, an object-based technique was applied to 74.5 hr of radar observation data to identify the size-sorting signatures in 10 nocturnal MCSs that were observed during the 2015 Plains Elevated Convective at Night (PECAN; Geerts et al. [2017]) field campaign. The magnitudes of these signatures are compared to various convective characteristics, emphasizing identifying trends between size-sorting magnitude, convective intensity, and precipitation intensity. To compliment the observational analysis, a numerical simulation of the MCS on 20 June 2015 during the PECAN campaign is also conducted to investigate the dependence of statistical trends on different microphysical processes. In summary, this study will address the following three scientific questions:

1. Are the magnitudes of hydrometeor size-sorting signatures in nocturnal MCSs statistically related to convective updraft characteristics?
2. If the hydrometeor size-sorting magnitudes are related to updraft strengths, what microphysical processes contribute the most to this relationship?
3. To what extent can we use hydrometeor size-sorting magnitudes to diagnose the relative contributions of microphysical processes to convective thermodynamics and precipitation pathway?

Table 1
List of the (Left Column) 10 Observed Nocturnal MCSs During the PECAN Field Campaign Analyzed in This Study, (Second Column) the Analysis Period for Each MCS, (Third Column) NEXRAD and SPolKa Radars Used to Generate Mosaics for Each MCS, and (Fourth Column) the Number of Size Sorting Objects Identified During the Analysis Period

Case	Analysis period (UTC)	Radar used in the mosaic	Number of size sorting objects identified
5 June 2015	5:00–11:00	KTWX, KEAX	270
11 June 2015	1:30–9:30	KUEX, KLNX, KOAX, KTWX	581
12 June 2015	4:00–10:00	KAMA, KDDC, KVNX, KTWX	535
17 June 2015	2:00–9:00	KUEX, KGLD, KLNX, KOAX	147
20 June 2015	3:00–9:30	KUDX, KBIS, KABR, KFSD	321
26 June 2015	2:30–10:30	KUEX, KOAX, KTWX, KEAX, KSGF	528
6 July 2015	1:30–7:00	KABR, KFSD	372
9 July 2015	2:00–9:00	KAMA, KFDR	695
14 July 2015	3:00–8:00	KDDS, KGLD, NCAR SPolKa	242
15 July 2015	0:00–9:00	KGLD, KDDC, NCAR SPolKa	305

2. Data Sources and Analysis Technique

2.1. Polarimetric Radar Observations

We utilized the level-II polarimetric products from the Next Generation Weather Radar (NEXRAD) WSR-88D network to examine hydrometeor size-sorting signatures in the convective regions from 10 nocturnal MCSs during the PECAN field campaign (Table 1). The S-PolKa radar, deployed during PECAN, was used in the composites for the two analyzed MCSs that entered its observation range on 14 July and 15 July 2015. NEXRAD radars performed regular plain position indicator (PPI) scans at 14 elevation angles, with a typical volume scan of 5–12 min. The Python ARM Radar Toolkit (Py-ART; Helmus & Collis [2016]) was used to merge radar observations onto a Cartesian grid with a horizontal grid spacing of 1 km and the vertical grid spacing of 0.5 km. The main radar parameters analyzed in this study are radar reflectivity (Z), differential reflectivity (Z_{DR}), and specific differential propagation phase (K_{DP}). Systematic biases in Z_{DR} observations were calibrated using the observations in radar-inferred dry aggregates, which are known to have very small Z_{DR} values (Ryzhkov & Zrnic, 1998; Zittel et al., 2014). The K_{DP} parameters were derived with the procedure outlined in Lang et al. (2007). The differential phase (ϕ_{DP}) was filtered with a 21-gate finite-impulse response filter, and the half slope of a line fitted to the filtered ϕ_{DP} was defined as the K_{DP}. Non-meteorological signal returns were removed with an insect-filtering algorithm (Lang et al., 2007) and a reflectivity texture-based ground-clutter removal algorithm (Gabella & Notarpietro, 2002). Radar gates with correlation coefficient (ρ_{hv}) values less than 0.8 were not included in the compositing procedure. Besides the systematic bias, Z_{DR} measurements can also be biased by non-uniform beam filling (NUBF) and depolarization streaks. These artifacts are most common at distant ranges and downstream of convective cells. Following Homeyer and Kumjian (2014), we mitigated these biases by merging radar observations taken at different locations and viewing angles into a range-weighted composite. To further reduce the contamination from the NUBF and depolarization streaks, observations that were not within 200 km from individual radars were discarded from the analysis.

2.2. WRF Simulations on Selected PECAN MCS Cases

The MCS on 20 June 2015 was simulated using Version 3.9 of the Weather Forecasting and Research (WRF; Skamarock et al. [2008]) Model. This case was chosen because of its leading-line trailing stratiform (LLTS) structure, which is one of the most common and well understood MCS archetype (e.g., Houze et al., 1989; Parker & Johnson, 2000). The simulation was performed with a triple-nested model domain with 27-, 9-, and 3-km grid spacing, respectively. Three WRF domains are shown in Figure 1. All domains contained 55 vertical levels, with greater vertical resolution near the melting level (~4 km) and boundary layer. The WRF model was initialized with the 32-km NCEP North American Regional Reanalysis (NARR; Mesinger et al. [2006]) data at 1500 UTC on 19 June and ran for 48 hr. The NARR wind (u, v) and temperature (T) fields above the boundary layer were

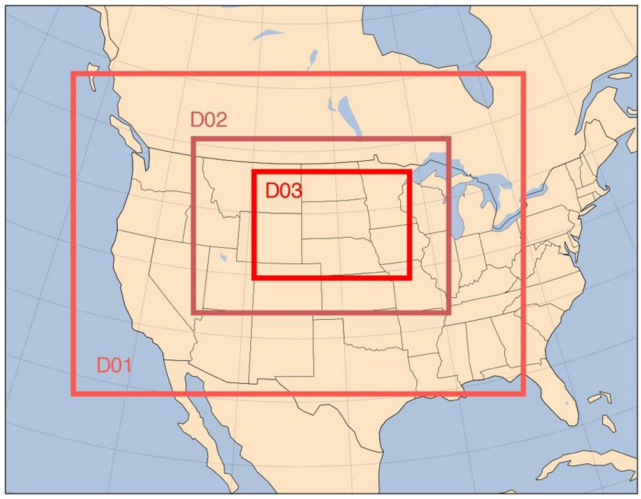

Figure 1. Domain setting used to simulate the 20 June 2015 MCS.

nudged every 3 hours for the first 30 hr of the simulation period to improve the representation of synoptic conditions. The model setting and physical parameterizations for the WRF simulation are listed in Table 2.

2.3. Object-Based Identification of Low-Level Size Sorting Signatures

The algorithm used to identify low-level size-sorting signatures in convective regions within MCSs is similar to that originally proposed for non-supercellular tornadic storms (Loeffler & Kumjian, 2018) and supercellular storms (Loeffler et al., 2020). We first identified the geometrical centers (i.e., the centroids) of different Z_{DR} and K_{DP} objects, that is, contiguous areas with enhanced Z_{DR} and K_{DP}, at 1-km height AGL. We used a 90-percentile magnitude threshold to produce "first guess" Z_{DR} and K_{DP} objects. These initial objects were adjusted manually to ensure that they accurately outlined local Z_{DR} and K_{DP} enhancements at scales of approximately 10–20 km within the MCS convective regions. The percentile thresholds used ranged from 90 (2.05 ± 0.35 dB for Z_{DR}; $0.69 \pm 0.27^{o}\text{km}^{-1}$ for K_{DP}) to 95 (2.45 ± 0.33 dB for Z_{DR}; $1.00 \pm 0.32\text{km}^{-1}$ for K_{DP}). We further applied a 75-percentile size threshold to remove objects smaller than 10 km. Finally, the centroid coordinates for each object were found and stored separately. While this method is inherently subjective, large variability in Z_{DR} and K_{DP} values in convective regions makes it difficult to determine a threshold that could identify Z_{DR} and K_{DP} objects at suitable spatial scales for all cases and all times (Martinaitis, 2017).

The second part of the algorithm involves matching different Z_{DR} and K_{DP} objects. A Z_{DR} object was matched to a K_{DP} object if it satisfies the following criteria:

1. the separation distance between the centroids was smallest for all object combinations, where the separation distance (d_{obs}) was the geometrical distance between the centroid of a Z_{DR} object ($x_{Z_{DR}}$, $y_{Z_{DR}}$) and the centroid of a K_{DP} object ($x_{K_{DP}}$, $y_{K_{DP}}$) as

$$d_{obs} = \sqrt{\left(x_{Z_{DR}} - x_{K_{DP}}\right)^2 + \left(y_{Z_{DR}} - y_{K_{DP}}\right)^2} \quad (1)$$

Table 2
List of WRF Grid Specification, Physical Parameterizations, Initial and Boundary Conditions Used to Simulate the 20 June 2015 MCS

Item	Outer domains	Innermost domain	References
Grid spacing	27 km, 9 km	3 km	
Domain dimensions	4185 × 4185, 2430 × 2430 km	1335 km × 1002 km	
Vertical sigma levels	55, 55	55	
Model top pressure	100 hPa, 100 hPa	100 hPa	
ICs and LBCs	NARR	NARR	
Microphysics	NSSL two-moment	NSSL two-moment	Mansell et al. (2010)
Cumulus parameterization	Kain-Fritsch	None	Kain (2004)
Longwave radiation	RRTM	RRTM	Mlawer et al. (1997)
Shortwave radiation	Dudhia	Dudhia	Dudhia (1989)
Surface layer	Eta similarity	Eta similarity	Janjic (1994)
Land surface model	Unified Noah	Unified Noah	Tewari et al. (2004)
Boundary layer physics	MYJ	MYJ	Janjic (1994)

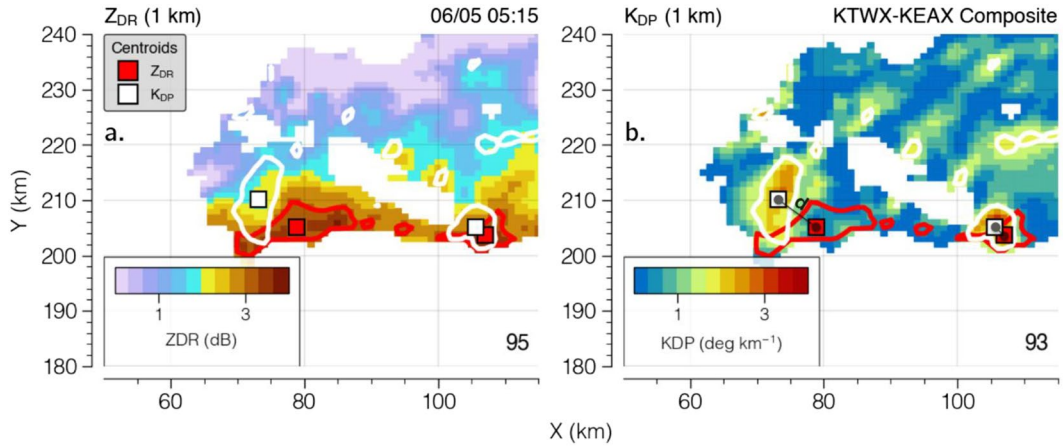

Figure 2. Example of size sorting object identification. Colored are radar observations of (a) Z_{DR} and (b) K_{DP} at 1 km. Red contours are the areas where Z_{DR} values exceed the 95th value percentile, white contours are the areas where K_{DP} values exceed the 93rd value percentile. For contour objects that also exceed a 75th size percentile, the contour centroids are marked with square markers. Separation distances at this time are represented by gray lines in Figure 2b.

2. for a Z_{DR} object, there was at least one K_{DP} object where the d_{obs} was less than 25 km; and (c) the angle between centroids was close to the direction of MCS movement. Separation distances (d_{obs}) were used herein as a quantitative measurement of size-sorting magnitudes. Matched Z_{DR} and K_{DP} objects are denoted as "size-sorting objects" hereafter

Figure 2 shows an example of size-sorting objects simultaneously identified at a particular time (0515 UTC on 5 June 2015) with the algorithm given above. The algorithm identified two areas with locally enhanced Z_{DR} and K_{DP} magnitudes near the system edge. The area near $X = 75$ km was of a large d_{obs}, whereas the area near $X = 105$ km was of a smaller d_{obs}. While there were several areas with enhanced K_{DP} in the rear of the system, these areas were filtered out because they were either too small or the Z_{DR} values near these K_{DP} areas did not exceed the magnitude threshold.

Since radar polarimetric products cannot be directly predicted by the WRF model, the WRF outputs are converted to Z_{DR} and K_{DP} equivalents with a radar simulator (Brown et al., 2016; Jung et al., 2010) to ensure a fair comparison between radar observations and model results. The WRF-equivalent separation distance (d_{WRF}) was defined as the geometrical distance between the centroids of the simulated Z_{DR} and K_{DP} objects.

2.4. Determining Local Characteristics Near Size-Sorting Objects

In the following sections, kinematics, microphysical and thermodynamic fields near the size-sorting objects were extracted and compared to their separation distances. To ensure representativeness at a convective scale, values collocated to a particular size-sorting object were the 75 percentile values of different variables within a 9-km diameter circle. The center of the circle was at the midpoint between Z_{DR} and K_{DP} centroids.

Since the collocation was performed at each time step, the output value represents the *instantaneous* measurement of each variable near each size-sorting object. This approach may be problematic for several reasons. First, the algorithm outputs may be biased against slower microphysical processes. Second, the algorithm outputs may misrepresent the "local characteristics" near sloped updrafts if the collocation was done in a point-to-point manner. The approach adopted in this study, which takes the environment surrounding each object into account, may minimize these uncertainties.

It is known that the thermodynamic structures of convective regions within MCSs are distinct from those of the stratiform regions (Braun & Houze, 1996; Gallus & Johnson, 1991). Hence, the relationship between local MCS

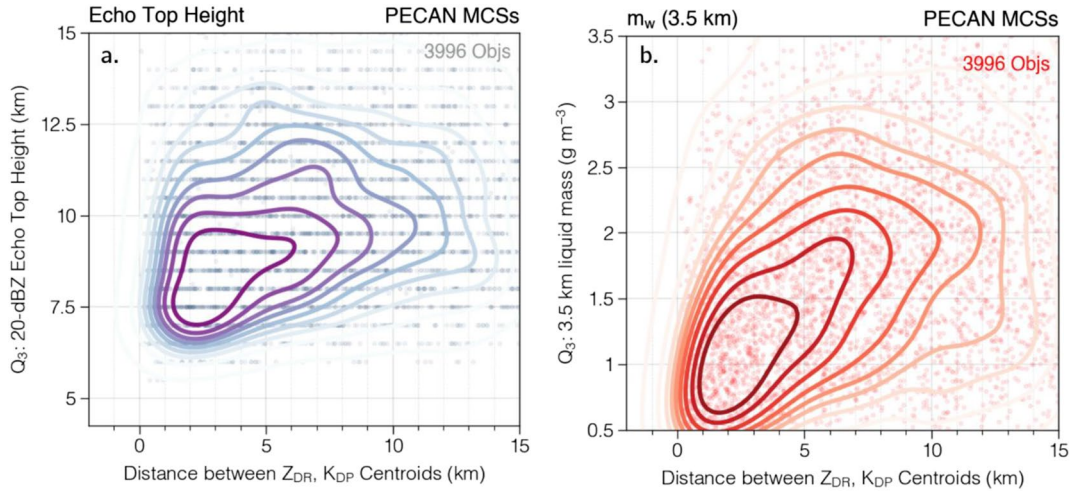

Figure 3. Plains Elevated Convection at Night mesoscale convective systems composite bivariate scatter distributions of the separation distance of each size sorting objects and (a) the collocated 75th percentile 20-dBZ Echo Top Height (km), (b) liquid water mass at 3.5 km. Superposed to the scatter plots are the normalized frequency distributions. The contours are at intervals of 0.11 from 0 to 0.99.

kinematics and d_{obs} (d_{WRF}) could be dependent upon their locations in the MCS. To remove this ambiguity, the radar reflectivity (Z)-based method of Steiner et al. (1995) was used to partition the radar data at 2-km height into convective and stratiform regions, and the parameters were tuned for convective systems over the Great Plains. All objects that were not within the convective regions were discarded from the analysis.

The size-sorting object dataset used herein consists of 3,996 objects that were identified from NEXRAD observations on 10 MCSs during the PECAN field campaign (Table 1). For the 20 June MCS simulated by the WRF, a total of 210 objects identified between 0600 and 1030 UTC was used to produce the statistical results shown in Section 5.

3. Statistical Characteristics of the Observed PECAN MCS Size-Sorting Objects

Figure 3a shows the bivariate distribution of PECAN MCS composite between separation distance (d_{obs}) and the 75th percentile values of 20-dBZ echo-top height (ETH) in the areas between the Z_{DR} and K_{DP} objects. ETH is used here as a proxy to answer our first research question on the relationship between size-sorting magnitude and updraft intensity. Scatter points represent the ETHs collocated to each object, whereas contours represent the normalized frequency distribution. The contours in Figure 3a show that objects with smaller d_{obs} were mostly associated with lower ETHs. The ETH versus separation distance (d_{obs}) distribution for each PECAN MCS indicates a large case-dependent variability, however. While 8 out of 11 PECAN MCSs exhibited increases in ETHs with the increasing d_{obs} (not shown), the d_{obs} magnitude where the ETH increase began and the increase rate varied between cases.

We now answer our second scientific question on whether d_{obs} can be used to infer microphysical variabilities. Since ETH is nonlinearly related to d_{obs}, we hypothesized that d_{obs} should reflect microphysical variabilities for two reasons: (a) greater positive buoyancy and latent heat release in stronger updrafts, and (b) higher amount of large ice hydrometeors in stronger updrafts, which could enhance cold rain processes (Lasher-Trapp et al., 2018).

Figure 3b shows the rain-mass (M_w) distribution at 3.5-km, or 0.5-km beneath the 4-km melting level. Choosing a vertical level slightly beneath the melting level enables a discussion on the contributions from melted hydrometeor to M_w. The M_w was derived from Z and Z_{DR} with the relationship by Cifelli et al. (2002),

$$M_w = 0.7 \times 10^{-3} Z^{0.886} \left(10^{Z_{DR}/10}\right)^{-4.159}. \quad (2)$$

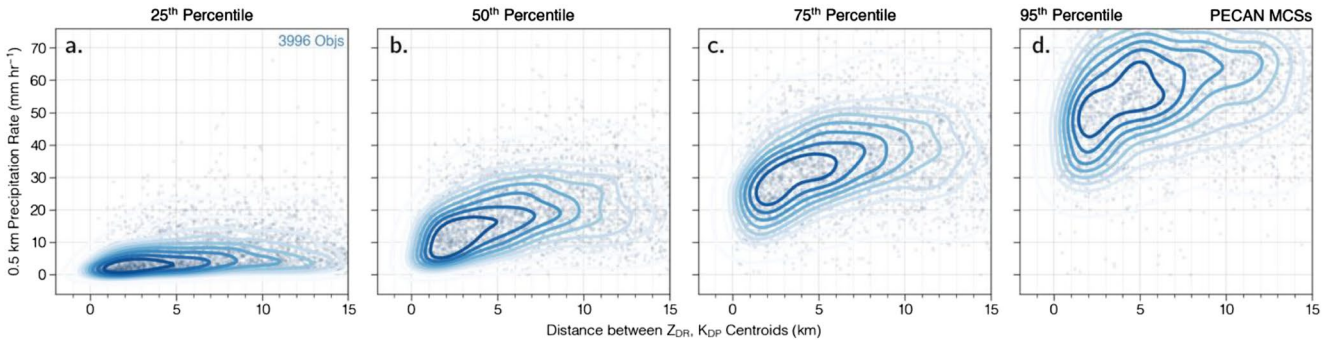

Figure 4. Same as Figure 3, but for (a) precipitation rates at 25th percentile, (b) precipitation rates at 50th percentile, (c) precipitation rates at 75th percentile, and (d) precipitation rates at 95th percentile. The contours are at intervals of 0.11 from 0 to 0.99.

It is clear in Figure 3b that the M_w at 3.5-km level increased non-linearly with d_{obs}, and the normalized frequency distribution for M_w rose rapidly for objects with d_{obs} of 0–8 km. For objects with $d_{obs} > 8$ km, the increase rate of M_w was more gradual than that for objects with $d_{obs} < 8$ km. Compared to the ETH distribution in Figure 3a, the M_w distribution at 3.5-km level is narrower at higher M_w values, suggesting less case-dependent variabilities.

To identify the type of precipitation which was most sensitive to the d_{obs}, the full statistical distributions between precipitation rates (R) and separation distance (d_{obs}) at 0.5-km height are shown in Figure 4. Precipitation rate (R) was derived at each radar gate with a blended algorithm that objectively chose different R estimations based on the magnitude of polarimetric variables (Cifelli et al., 2011). Figure 4a shows that R changed little with the increasing d_{obs} at 25th percentile. A nonlinear increase in R with the increasing d_{obs} can be identified at larger percentiles (Figures 4b–4d), however. At 75th percentile (Figure 4c), R rose at a rapid rate for d_{obs} of 0–8 km and rose at a more gradual rate for $d_{obs} > 8$ km.

While the raindrops associated with mixed-phase and ice microphysics ("cold rain") cannot be directly distinguished from warm rain, the contribution of ice-phase microphysics to R likely peaks at or slightly beneath the melting level (Jensen et al., 2018; Kain et al., 2000; Yang & Houze, 1995). Thus, we inferred from Figure 3b that the ice- and mixed-phase microphysics could be producing more M_w near large d_{obs} objects. The similarity between M_w and R distributions at high percentiles in Figures 4c and 4d also implies that the greater likelihood of intense precipitation near large d_{obs} objects may be attributable to the ice- and mixed-phase microphysical processes. These inferences will be discussed further with WRF simulation in Sections 5 and 6.

4. Validating the Simulated 20 June 2015 MCS With Observations

4.1. MCS Track and Morphology

Figure 5 compares the temporal evolution of the vertical column-maximum radar reflectivity between the observation and WRF simulation from 0600 UTC to 1100 UTC on 20 June 2015. The observed MCS was initially located in central South Dakota at 0600 UTC and propagated eastward in the next 5 hrs. The observed movement of this MCS (Figures 5f–5j) was reproduced reasonably well by the WRF simulation (Figures 5a–5e). Both the simulated and observed MCSs were of the LLTS archetype. There were certain times when the observed and simulated MCSs were structurally different. For example, the observed MCS at 0600 UTC (Figure 5f) consisted of a bow echo and two secondary convective lines northeast and southwest of the bow echo. While the WRF produced a bow echo with similar orientation to the observed (Figure 5a), the simulated northeastern secondary line was less organized than the observed. The morphological differences disappeared after 0700 UTC (Figures 5b and 5g), as the simulated northeastern line grew upscale and merged with the bow echo.

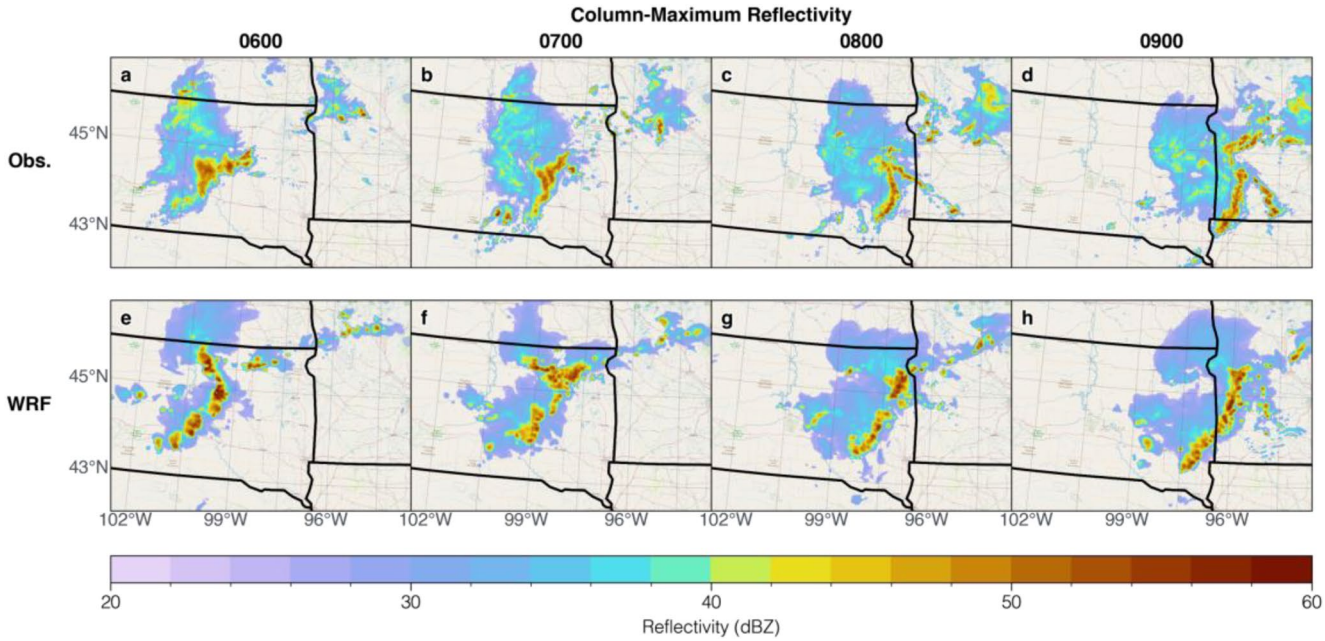

Figure 5. Model validation of the 20 June mesoscale convective system (MCS). The upper row shows the simulated column-maximum reflectivity maps, valid at (a) 0600 UTC, (b) 0700 UTC, (c) 0800 UTC, and (d) 0900 UTC. The simulated MCS evolution is compared to the next generation weather radar reflectivity mosaic (lower row; e, f, g, h), valid at the identical times as those shown for the weather forecasting and research simulation.

4.2. Convective Echo Structure

Figure 6 compares the observed and simulated contoured frequency by altitude diagrams (CFADs; Yuter & Houze, 1995a) of radar reflectivity (*Z*) for convective pixels identified with the Steiner et al. (1995) convective-stratiform partition method during the mature phase of the 20 June MCS. The mature phase for the 20 June MCS was defined as periods with steady mean 20 dBZ echo-top heights (0600–1000 UTC). For this comparison, we track how the highest frequency contours in each CFAD change at different vertical levels. Since *Z* is a function of hydrometeor diameter and number concentration, its vertical gradient contains information on how microphysical processes evolve in the vertical.

The CFAD of observed *Z* in the convective region (Figure 6a) contains three areas of interest. The first is the steady increase in *Z* with decreasing altitude beneath 4 km. Warm layer *Z* enhancement is indicative of warm rain

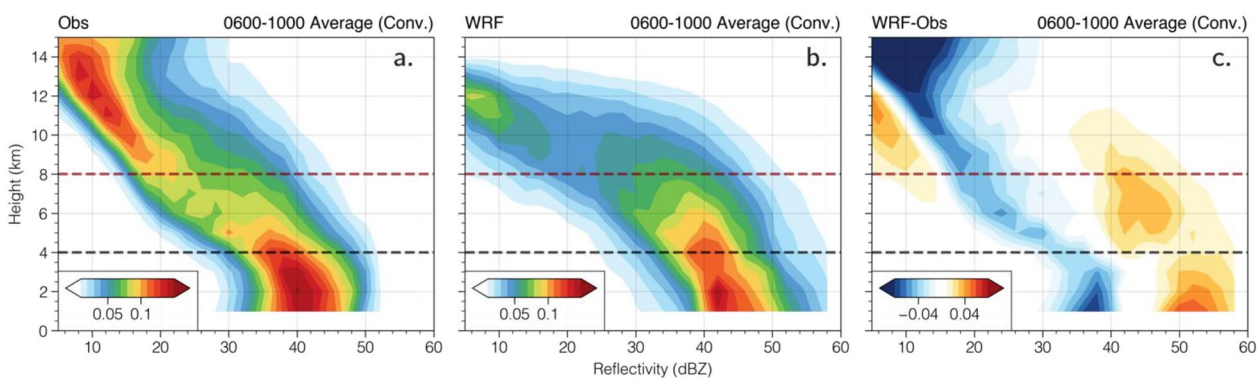

Figure 6. Reflectivity echo structural validation. Panels show the (a) observed reflectivity contoured frequency by altitude diagrams (CFAD) and (b) weather forecasting and research (WRF)-simulated reflectivity CFAD during the mesoscale convective system mature phase (0600–1000 UTC), and (c) the difference between the WRF-simulated and observed reflectivity. Grid values that were not flagged as convective echoes with the Steiner et al. (1995) convective-stratiform partition algorithm were omitted from analysis. 4-km (black dashed) and 8-km (red dashed) heights are highlighted for easier comparison with the text.

Table 3
The Change of Radar Reflectivity With Altitude (dZ/dz; dBZ km^{-1}) in Three Vertical Layers (2–4 km, 4–8 km, and 8–14 km, Repsectively)

		dZ/dz (dBZ km^{-1})	
	Layer	Observed	WRF
Mature	2–4 km	−1.55	−1.82
	4–8 km	−2.80	−2.46
	8–14 km	−2.61	−5.71
Weakening	2–4 km	−1.66	−2.21
	4–8 km	−3.80	−3.51
	8–14 km	−1.80	−4.43

Note. Shown are the observed dZ/dz and the WRF-simulated dZ/dz during the MCS mature and weakening phases.

processes, that is, collision-coalescence of rain (Kumjian and Prat, 2014). The second is the Z increase with decreasing altitude between the melting level (4 km) and 8 km. Z increase in this layer is related to mixed phase growth. The third one is the modest decrease in Z above 8 km. The main difference of Z CFAD between the observed (Figure 6a) and the simulated (Figure 6b) is that the Z reduction above melting level occurs at a much higher altitude in the simulated MCS. This error resulted in a ∼10 dBZ for Z overestimation between 8 and 10 km. The overestimation of Z at upper levels (above 8 km in this case) is common for cloud-resolving simulations of deep convective systems (e.g., Bodine and Rasmussen, 2017; Stanford et al., 2017; Varble et al., 2011; Varble et al., 2014; Wu et al., 2013). Stanford et al. (2017) attributed upper-level Z overestimation to ice size bias in low temperatures. Another potential cause of this bias is overpredicted hydrometeor lofting in convective updrafts. Despite this bias, the simulated and observed Z CFADs were comparable below 8 km. Specifically, the simulated change rates of Z beneath the melting level and 4–8 km were both within 20% of the observed values (Table 3).

4.3. Spatial Correspondence Between Size-Sorting Signatures and Low-Level Flow Directions

To verify whether the WRF model produced size-sorting signatures or not, we compared the simulated mass-mean rain diameter versus rain concentration (D_{mr}-N_{Tr}) distributions at the lowest model level at 0720 UTC (Figures 7d–7f) to the observed Z_{DR}-K_{DP} distributions at 1-km height at 0620 UTC (Figures 7a–7c). The timing difference was to account for the 1-hr delay in the merger of the secondary line with the main MCS. Radial velocity measurements from two NEXRAD radars (KABR and KFSD) were used to retrieve ground-relative winds (u_g, v_g) and vertical wind (w). We then calculated the system-relative wind (u_r, v_r) by subtracting the MCS movement vector (u_{MCS}, v_{MCS}) from ground-relative winds. MCS movement was determined by tracking the movement of the centroids of the closed 20-dBZ contours from 0300 to 1200 UTC. The movement vector of the MCS (u_{MCS}, v_{MCS}) was determined to be (26.1, −1.35) m s^{-1} for the observed 20 June MCS, and (24.5, −1.67) m s^{-1} for the simulated MCS, respectively.

Figures 7b and 7c show that for the observed MCS, the enhancements in K_{DP} were located downwind of both the Z_{DR} enhancements and updrafts. The angle between Z_{DR} and K_{DP} enhancements roughly paralleled the system-relative inflow. These observed spatial patterns were reproduced in the WRF simulation (Figures 7d and 7f). For example, two areas with larger D_{mr} could be found near X = 900 km and X = 913 km, and downwind of these D_{mr} enhancements and updrafts were two isolated areas with enhanced N_{Tr} near X = 885 km and X = 900 km in Figure 7f. In the next section, we will use the simulated MCS to discuss the thermodynamic and microphysical implications of size sorting signatures.

5. Low-Level Size-Sorting Signatures in the WRF-Simulated 20 June 2015 MCS

5.1. Statistical Relationship Between Convective Height and Size Sorting Effect

Bivariate distributions of ETH versus separation distance for the observed and simulated MCSs on 20 June 2015 are shown in Figures 8a and 8b, respectively. WRF underestimated the separation distances in the 20 June MCS (Figures 8a and 8b). The simulated ETH-d_{WRF} bivariate distribution also contains a subset of small-d_{WRF}, large ETH objects (Figure 8b). We cannot identify such objects in the observed distribution (Figure 8a). Despite these differences, critical characteristics of the observed ETH-d_{obs} distribution were retained in the WRF simulation, namely the shift toward higher ETHs with increasing d_{WRF} magnitudes (Figures 8a and 8b). This suggests that WRF captured the main statistical correlation between the observed separation distances (d_{OBS}) and the ETHs.

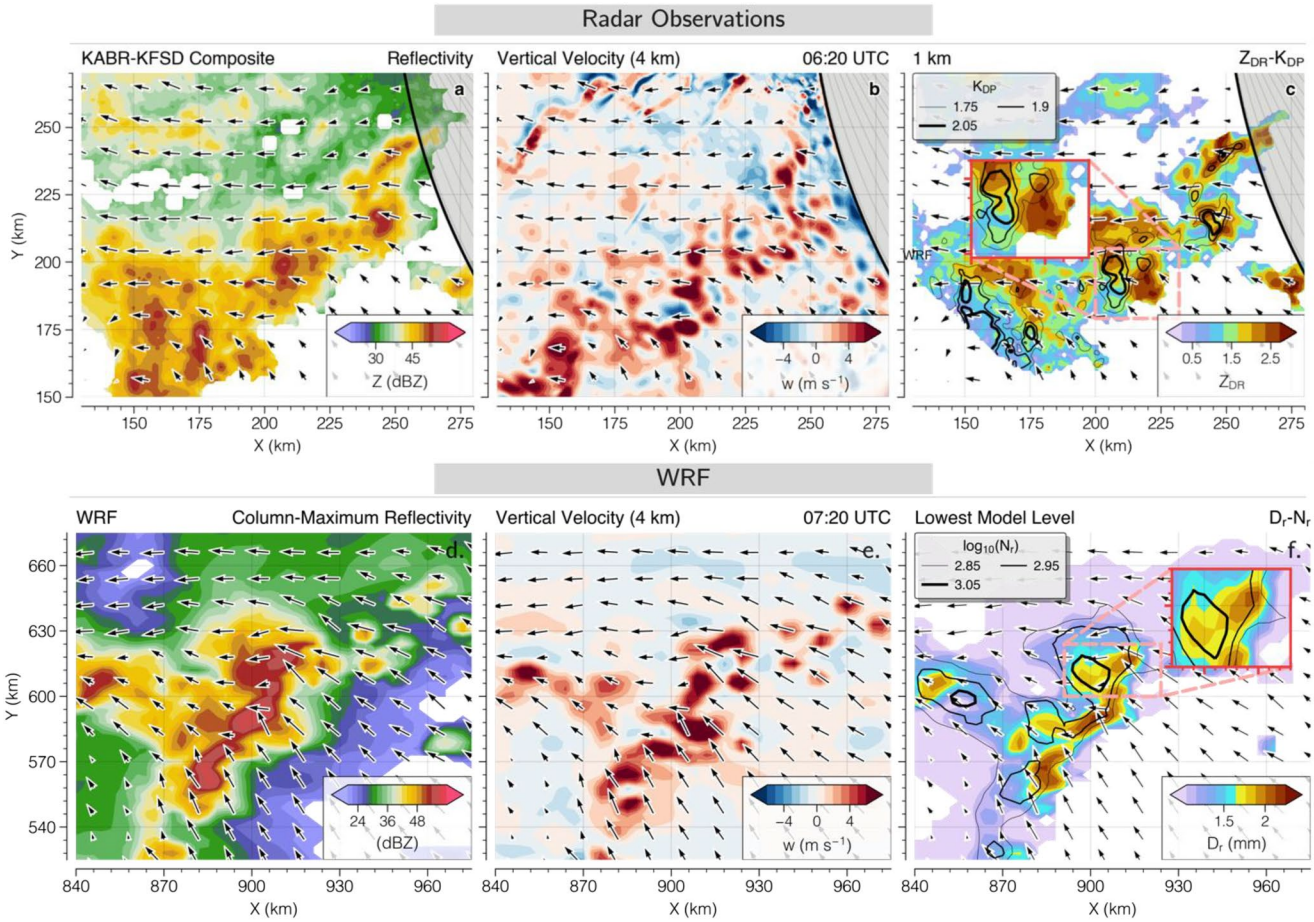

Figure 7. Validating size sorting process in the weather forecasting and research (WRF) simulation. Upper row shows the KABR-KFSD composite of (a) column-maximum reflectivity, (b) 4 km vertical velocity retrieved from KABR-KFSD radial velocities, (c) 1 km Z_{DR} (color; dB) and K_{DP} (yellow contours; plotted at 1.75, 1.9, and 2.05 deg km^{-1}). Vectors in panels (a)–(c) are the mean low-level (1–4 km) system-relative winds. Gray shading in panels (a)–(c) are the KABR-KFSD dual-doppler lobes, where dual-doppler winds cannot be retrieved. Panels in the lower panel (d)–(e) are similar to panels (a)–(b), but for the WRF simulation. Panel (f) shows the (color) rain diameter and (contour) rain concentration at logarithmic scale, both valid at the lowest model level.

5.2. Statistical Relationship Between Size Sorting Effect and Microphysical Properties

Figure 8c shows the bivariate distribution of d_{WRF} versus ice/liquid water path (IWP/LWP). The normalized d_{WRF}– IWP bivariate frequency distribution (blue contours in Figure 8c) shifts to higher IWP magnitudes as d_{WRF} increase. On the other hand, normalized d_{WRF}– LWP bivariate frequency distribution (orange contours in Figure 8c) shows no appreciable trend with increasing d_{WRF} up to 6 km and trends slightly toward lower LWP magnitudes when d_{WRF} increases beyond 6 km.

A reasonable question to ask is whether or not the surface precipitation is also correlated to d_{WRF}. We separated the simulated size-sorting objects into two categories that are roughly the same sample size. The first category contained objects with d_{WRF} smaller than the median d_{WRF} of 4.5 km, whereas the second category was for objects with $d_{WRF} > 4.5$ km. The statistical distributions of R for the two object categories during the MCS mature phase are compared in Figure 9. The statistical distributions of R for these two object categories were very similar for weaker precipitation rate ($R < 60$ mm hr^{-1}). However, large d_{WRF} objects are more likely to produce *intense* precipitation ($R > 60$ mm hr^{-1}; strongest 19% of the R samples) than the small d_{WRF} objects.

Figure 8c shows that more ice and mixed phase hydrometeors were produced near the large d_{WRF} objects. The sedimentation and subsequent melting of these ice particles are hypothesized to contribute to the greater likelihood of intense rainfall near large d_{obs} & d_{WRF} objects. We will evaluate this hypothesis with vertical profiles of different rain-mass components in Section 6.

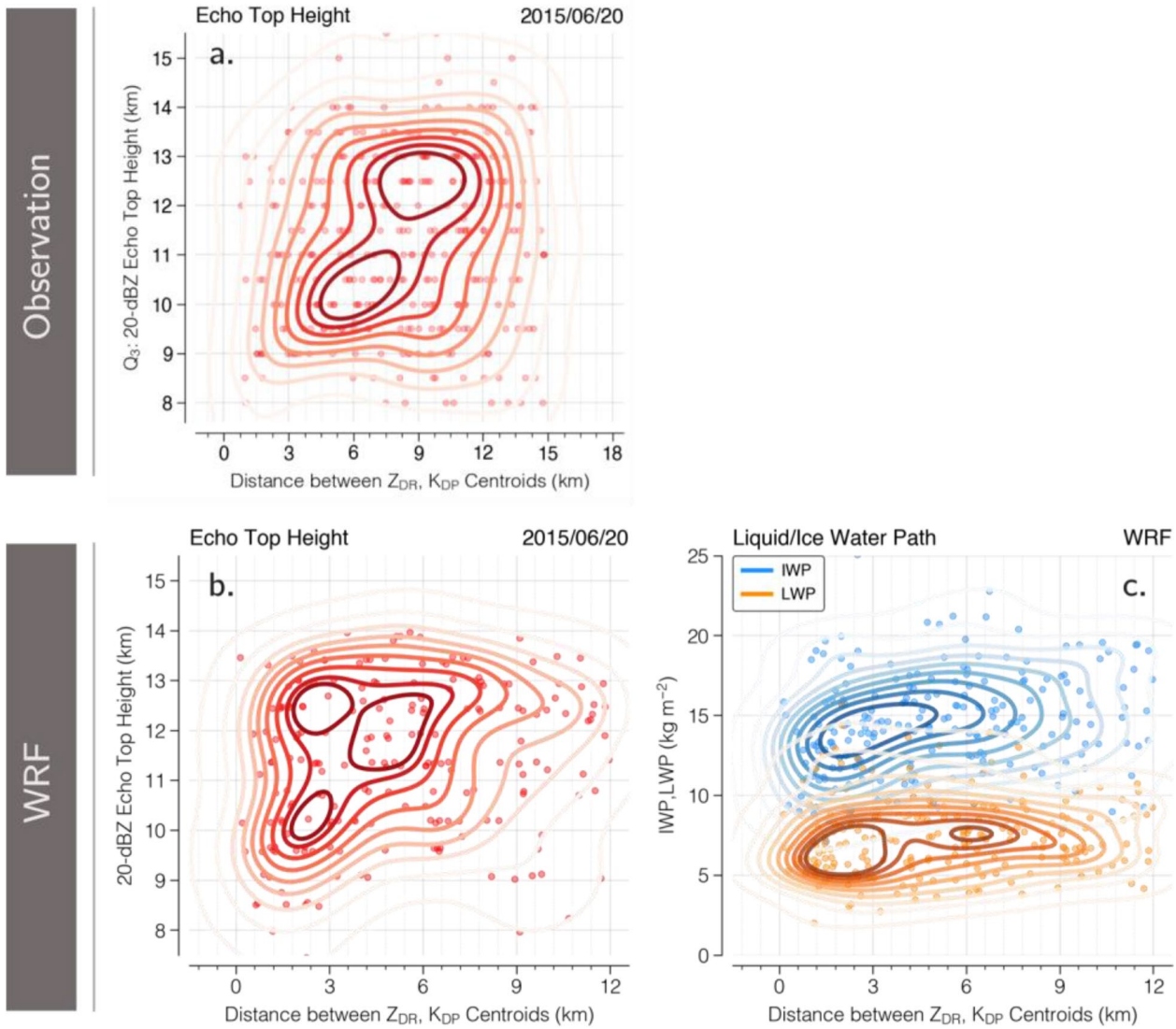

Figure 8. (a) Separation distances versus Echo Top Heights bivariate scatters and normalized frequency distribution for the observed 20 June 2015 mesoscale connective scale. (b) Simulated bivariate scatters and normalized frequency distribution of separation distances and echo top heights. (c) Simulated bivariate scatters and normalized frequency distribution of ice water path (IWP; blue scatters and contours) and liquid water path (LWP; orange scatters and contours). All frequency contours are at intervals of 0.11 from 0 to 0.99.

5.3. Statistical Relationship Between Size Sorting Effect and Thermodynamic Characteristics

In this subsection, the latent heating and cooling terms from the WRF model were grouped into six essential microphysics components (deposition, freezing, condensation, sublimation, melting, and evaporation). To minimize uncertainties in the vertical, d_{WRF} were compared to the vertically-integrated values of each microphysics component.

Figures 10a–10c show the bivariate distributions of three latent heating terms. Notice that the vertically-integrated latent heating and cooling terms in the *y*-axis in Figure 10 were displayed in logarithmic scales. The integrated condensation heating rates ($\int P_{Cond}$; Figure 10c) were about half an order magnitude higher than the deposition rates ($\int P_{Dep}$; Figure 10a), and an order magnitude higher than the freezing rates ($\int P_{Frz}$; Figure 10b), respectively. The dominant role of condensation in the convective regions is consistent with simulations on two MCSs during the Midlatitude Continental Convective Clouds Experiment (MC3E; Jensen et al. [2018]) by Marinescu et al. (2016). The $\int P_{Cond}$ and $\int P_{Dep}$ were insensitive to separation distance $\left(d_{WRF}\right)$, with most size-sort-

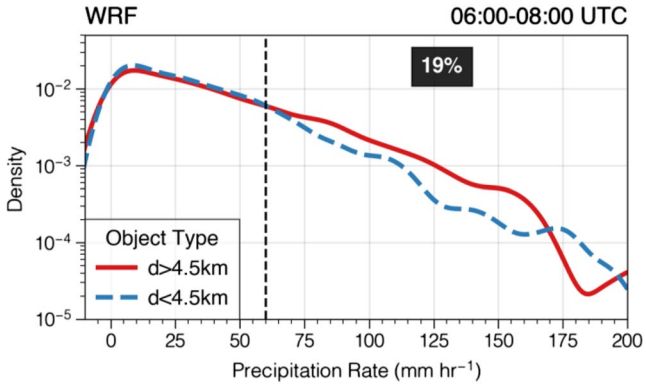

Figure 9. Probability density functions (PDFs) of the precipitation rates near size sorting objects with $d_{WRF} > 4.5$ km (red solid line) and those near size sorting objects with $d_{WRF} < 4.5$ km during the mesoscale connective scale mature phase (i.e., 0600–1000 UTC). Text box in the figure shows the percentage of samples with precipitation rates greater than 60 mm hr^{-1}.

ing objects having very similar integrated condensation and deposition rates aloft (Figures 10a and 10c). In contrast, the distance of $\int P_{Frz}$ (Figure 10b) was similar to the ETH and IWP distributions (Figures 8b and 8c) in showing a nonlinear increase trend with separation distance (d_{WRF}).

The distributions of three latent cooling terms are shown in Figures 10d–10f. There were no noticeable trends in vertically-integrated sublimation ($\int P_{Sub}$; Figure 10d) and evaporation ($\int P_{Evap}$; Figure 10f), suggesting that the net cooling from these two processes were insensitive to d_{WRF}. In contrast, there was a slight tendency for the integrated melting cooling ($\int P_{Melt}$; Figure 10e) to become more negative, that is, stronger, with increased d_{WRF}. In particular, the shape of the $\int P_{Melt}$ versus d_{WRF} distribution was similar to those of the ETH, IWC, and $\int P_{Frz}$ but inverted.

The similarity between the $\int P_{Frz}$ and $\int P_{Melt}$ distributions to those of the ETH and IWP supports our finding in Section 4b on more active ice/mixed phase processes near large d_{WRF} objects. From Figure 10, we conclude that both the integrated freezing heating and melting cooling vary with d_{WRF}. On the other hand, the integrated latent heat release/absorption through condensation, deposition, and evaporation are less sensitive to d_{WRF}.

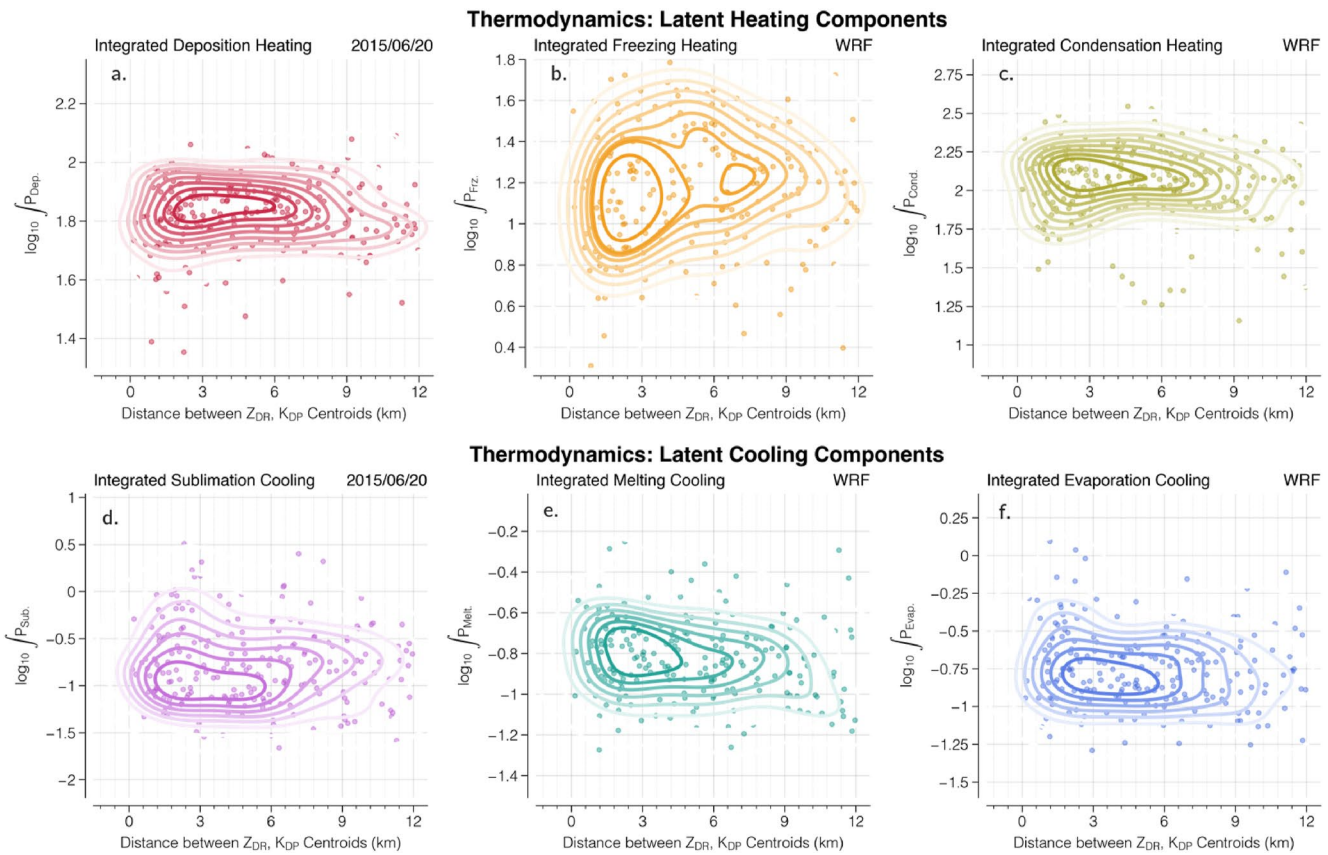

Figure 10. Simulated bivariate distributions of separation distances and integrated microphysical heating/cooling terms. Panels in the upper row show the object-collocated values (scatters) and the normalized frequency distributions of (a) integrated deposition heating, (b) integrated freezing heating, and (c) integrated condensation heating. Panels in the lower row are for the three integrated cooling terms, including (d) integrated sublimation cooling, (e) integrated melting cooling, and (f) integrated evaporation cooling. All frequency contours are at intervals of 0.11 from 0 to 0.99.

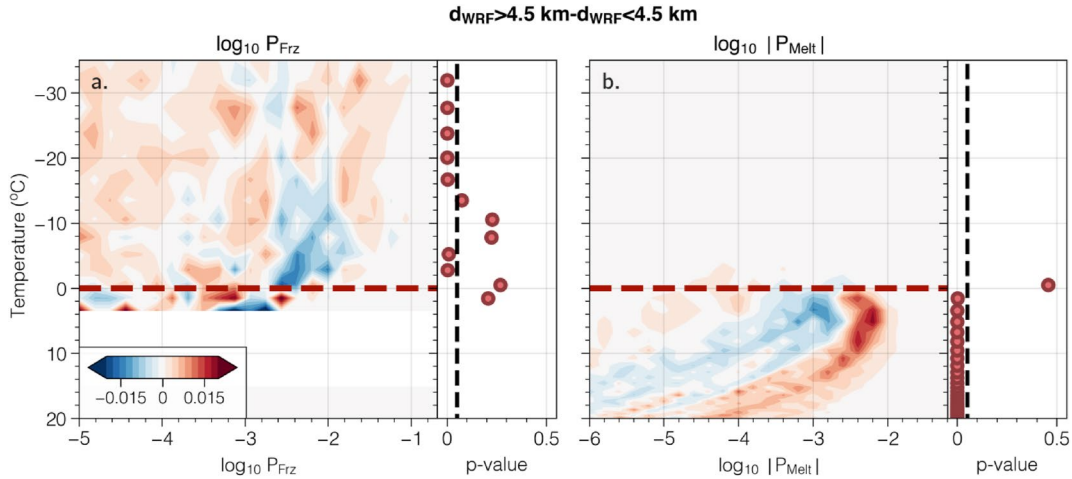

Figure 11. The differences between the contoured frequency by altitude diagrams for $d_{WRF} > 4.5$ km objects and objects with $d_{WRF} < 4.5$ km objects and the two-sample K-S test p-values at different temperature levels. The variable analyzed in panel (a) is the freezing heating, in logarithmic scale, whereas the variable analyzed in panel (b) is the logarithmic scale melting cooling. Black dashed vertical lines in the K-S p-value panels represent the K-S significant threshold, that is, p-value less than 0.05.

5.4. Statistical Differences in Thermodynamic Profiles

While bivariate distributions in Figure 10 elucidated some statistical relationships between local thermodynamics and separation distance (d_{WRF}), some ambiguities remain. Detailed information in the vertical is lost in the vertical integration. This produces some uncertainties in the interpretation of flat bivariate distributions in Figure 10.

Differences in statistical characteristics in the vertical are illustrated in this section with CFAD differences between objects of the two ETH-d_{WRF} categories. The CFADs are calculated from the 9-km diameter circular area surrounding each object. The signs of the contours on the right-hand-side (RHS) of the CFAD difference figures (Figures 11–14) are critical to the interpretation herein. Since CFADs show how the probability distributions of a variable evolve in the vertical, positive (negative) difference to the right of Figures 11–14 means that the magnitudes of the variable will be larger near the large (smaller) d_{WRF} objects.

Since the CFAD difference figures are noisy, we used the Kolmogorov-Smirnov two-sample test (K-S test; Massey, 1951; Kolmogorov, 1933; Smirnov 1939) to identify the temperature levels where the CFAD differences are statistically significant. The K-S test is a non-parametric test that determines if two samples have the same underlying distribution. The null hypothesis that the two samples are taken from the same statistical distribution is rejected with p-values less than 0.05. The CFAD differences at different temperature levels were deemed not statistically significant if the K-S p-values were greater than 0.05. The same statistical method was adopted by Stechman et al. (2020b) to discuss the differences between airborne in-situ microphysical measurements gathered in the transition zones and stratiform regions of different PECAN MCSs.

Figure 11 shows the CFAD differences for the freezing and melting terms, which are nonlinearly related to d_{WRF} when vertically integrated (Figures 10b and 10e). The temperature ranges where the CFAD differences were statistically significant are between −32°C and −15°C for freezing, and between 2 and 20°C for melting. Within these temperature ranges, there were stronger freezing and cooling near the large d_{WRF} objects.

For other four latent heating or cooling terms (deposition heating, condensation heating, sublimation cooling, and evaporation cooling) in Figure 12, CFAD differences at different temperature ranges roughly offset each other when vertically integrated. The following differences were shown to be statistically significant:

1. Stronger evaporation near the large d_{WRF} objects below the melting level (0°C; Figure 12d)
2. Stronger sublimation near the large d_{WRF} objects from −25°C to −32°C (Figure 12c)
3. Weaker deposition near the large d_{WRF} objects from –5°C to −18°C, and weaker condensation near the large d_{WRF} objects within temperature range from 0 to 8°C (Figures 12a and 12b)

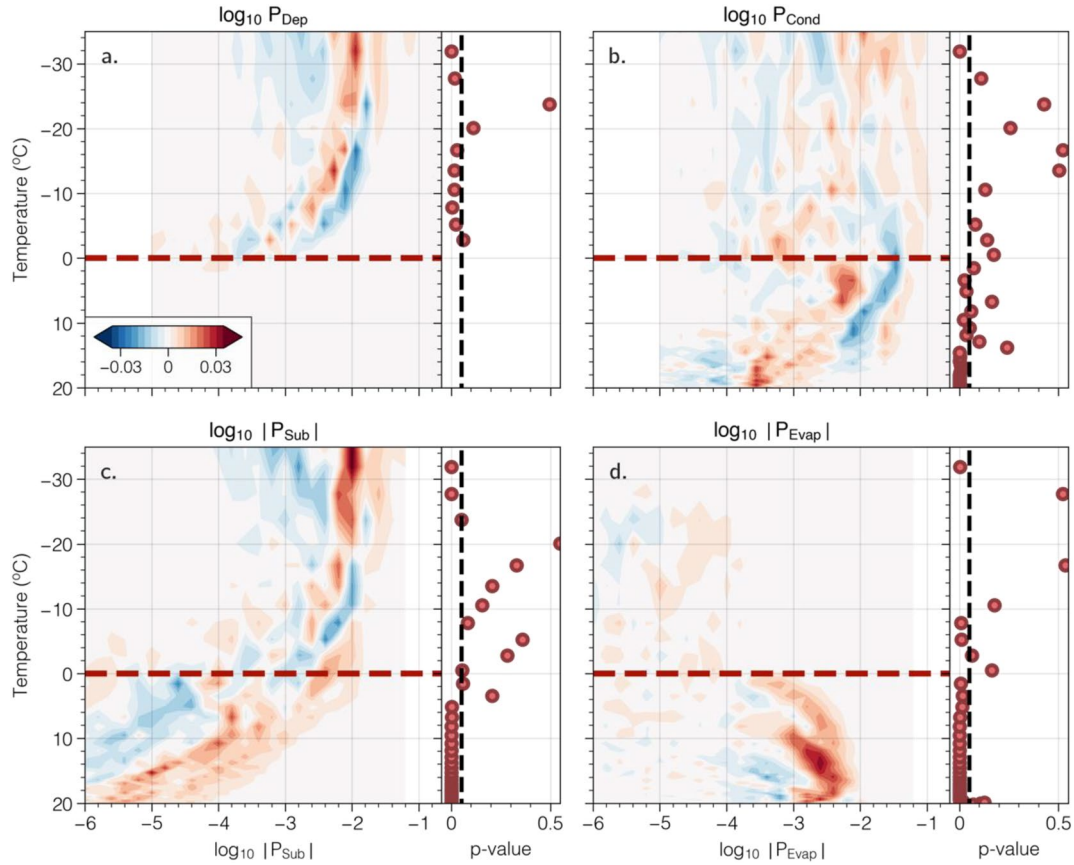

Figure 12. Similar to Figure 11, but for (a) deposition heating, (b) condensation heating, (c) sublimation cooling, and (d) evaporative cooling. All heating and cooling terms are in logarithmic scale.

5.5. Implications of the Thermodynamic Variabilities on Kinematics

While ETH reveals correlation between convective kinematics and separation distance (d_{WRF}), two questions remained unanswered. First, are the deeper echoes near large d_{WRF} objects tied to updrafts at lower, middle, or upper levels? Second, is the correlation statistically significant? Vertical motion (w) in updrafts is determined by the buoyancy and pressure gradient force (Peters, 2016). While latent heat release during phase change can make

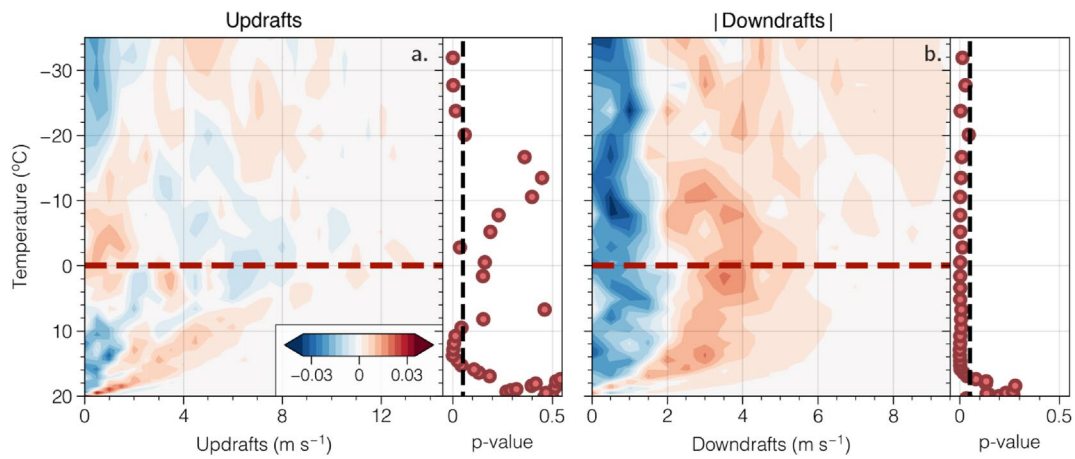

Figure 13. Similar to Figure 12, but for (a) updraft intensity and (b) downdraft intensity.

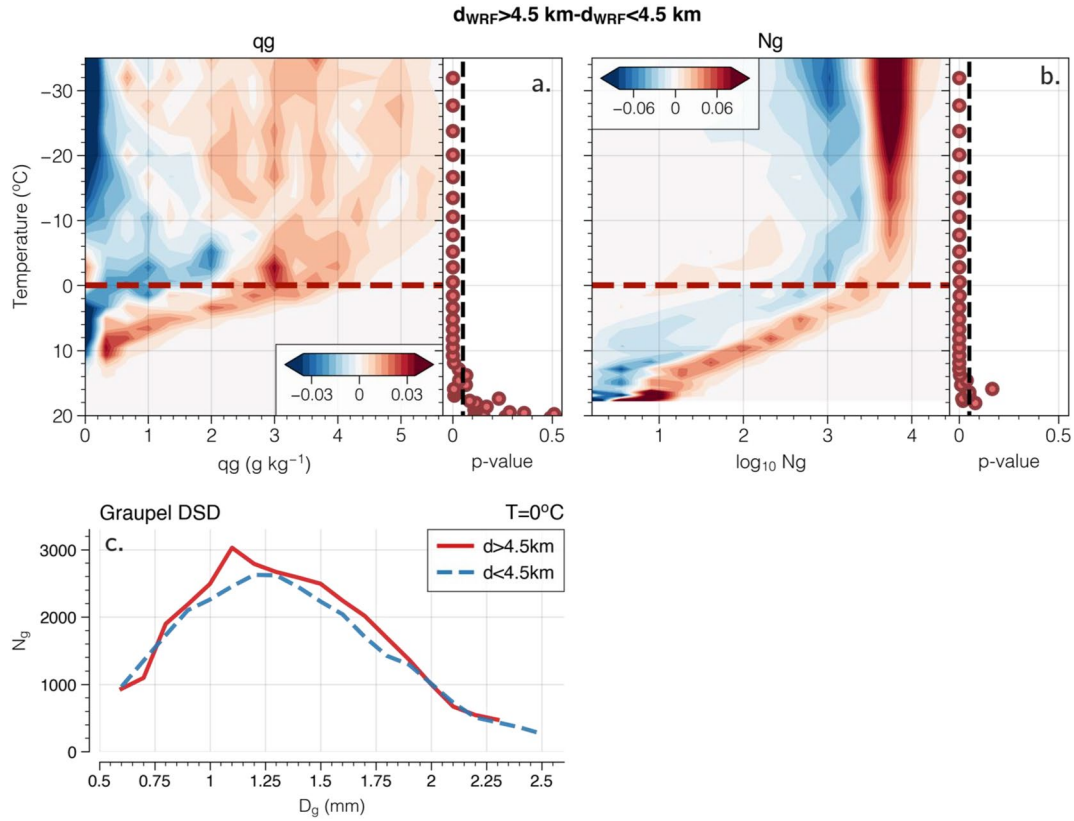

Figure 14. Similar to Figure 12, but for (a) graupel mixing ratio and (b) graupel number concentration in logarithmic scale. (c) Graupel drop size distribution at 0 °C for $d_{WRF} > 4.5$ km objects (red solid line) and $d_{WRF} < 4.5$ km objects (blue dashed line).

the air parcel more buoyant, whether the increased buoyancy translates to stronger w is dependent upon updraft slopes (Parker, 2010) and widths (Morrison, 2016; Peters, 2016). Furthermore, factors like hydrometeor loading and entrainment can also impact w (e.g., Storer & van den Heever, 2013; Tao et al., 1995).

Figure 13 shows the difference between the updraft and downdraft CFADs of the two object categories. The large d_{WRF} objects contain stronger updrafts beneath the melting level and at upper levels (Figure 13a). Downdrafts near large d_{WRF} objects are stronger than those near small d_{WRF} objects over all temperature values (Figure 13b). Similarly, Figure 14 shows the CFAD difference between the mixing ratio and concentration of graupel particles of two object categories, as well as the graupel DSD at the melting level for the two object categories.

Not all kinematic characteristics identified in Figure 13 pass the K-S significance threshold. A clear link between downdraft and d_{WRF} is confirmed as the p-values for downdrafts were mostly smaller than 0.05. In contrast, most updraft differences either only marginally satisfy or fail to pass the K-S significance threshold altogether (Figure 13a). One of the temperature ranges where the updraft differences passed the K-S threshold was between −20°C and −32°C, a temperature range that contained statistically significant freezing enhancement near large d_{WRF} objects (Figure 11a).

5.6. Spatial Similarities Between Graupel Sedimentation Patterns and Size Sorting Signature

This section discusses the composite spatial distributions of different variables near size-sorting objects. Spatial distributions corresponding to each object were first interpolated to the polar coordinate and rotated so that the prevalent wind directions were fixed easterly. Here, we compare D_{mr} and N_{Tr} at the lowest model level (Figures 15c and 15d), D_{mg} and N_{Tg} at 4 km (Figures 15a and 15b), and vertical velocity at 4 km (Figure 16a). These heights were chosen to reflect graupel DSD at the melting level (4 km) and rain DSD close to the surface. The composited

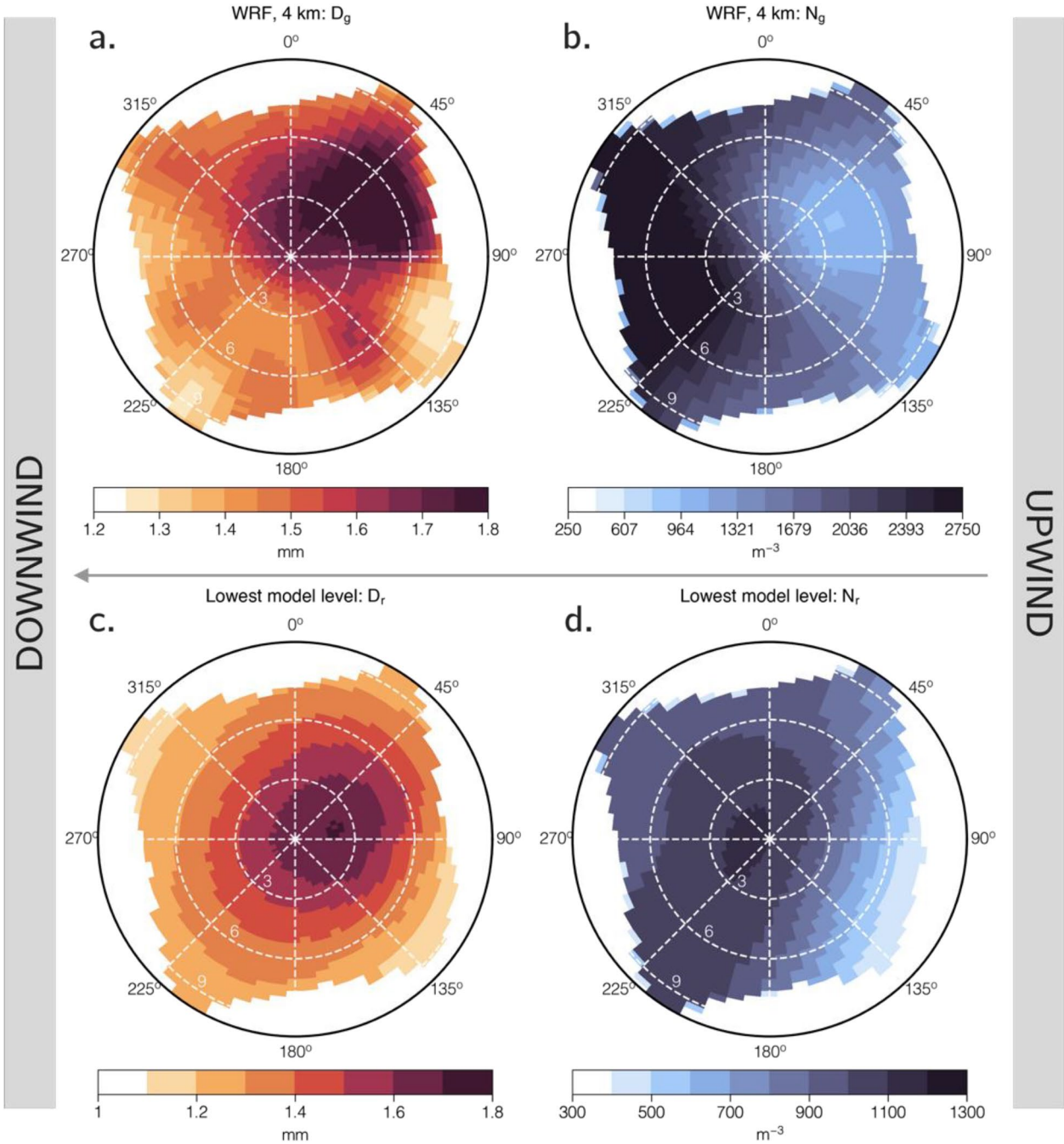

Figure 15. Simulated mean spatial distributions of different variables at different heights in the 12 km diameter circles surrounding the midpoint between D_{mr} and N_{Tr} centroids, shown in polar coordinates. The variables analyzed in each panel is (a) graupel diameter at 4 km, (b) graupel number concentration at 4 km, (c) rain diameter at 0.25 km, and (d) rain number concentration at 0.25 km. The figures are constructed in a way so that the right hand side of each panel is the upwind side, whereas the left hand side of each panel is the downwind side.

D_{mr} was located in the upwind (i.e., right-hand) side of Figure 15d, whereas N_{Tr} was located in the downwind (i.e., left-hand) side of Figure 15e. A clear spatial separation between graupel diameter (D_{mg}; Figure 15a), and graupel number concentration (N_{Tg}; Figure 15b) can be observed. Larger, but less numerous, graupel particles were distributed in the upwind side and were fairly close to the strongest updrafts (Figure 16a). In contrast, smaller, but more numerous, graupel were located in the downwind side of Figure 15b.

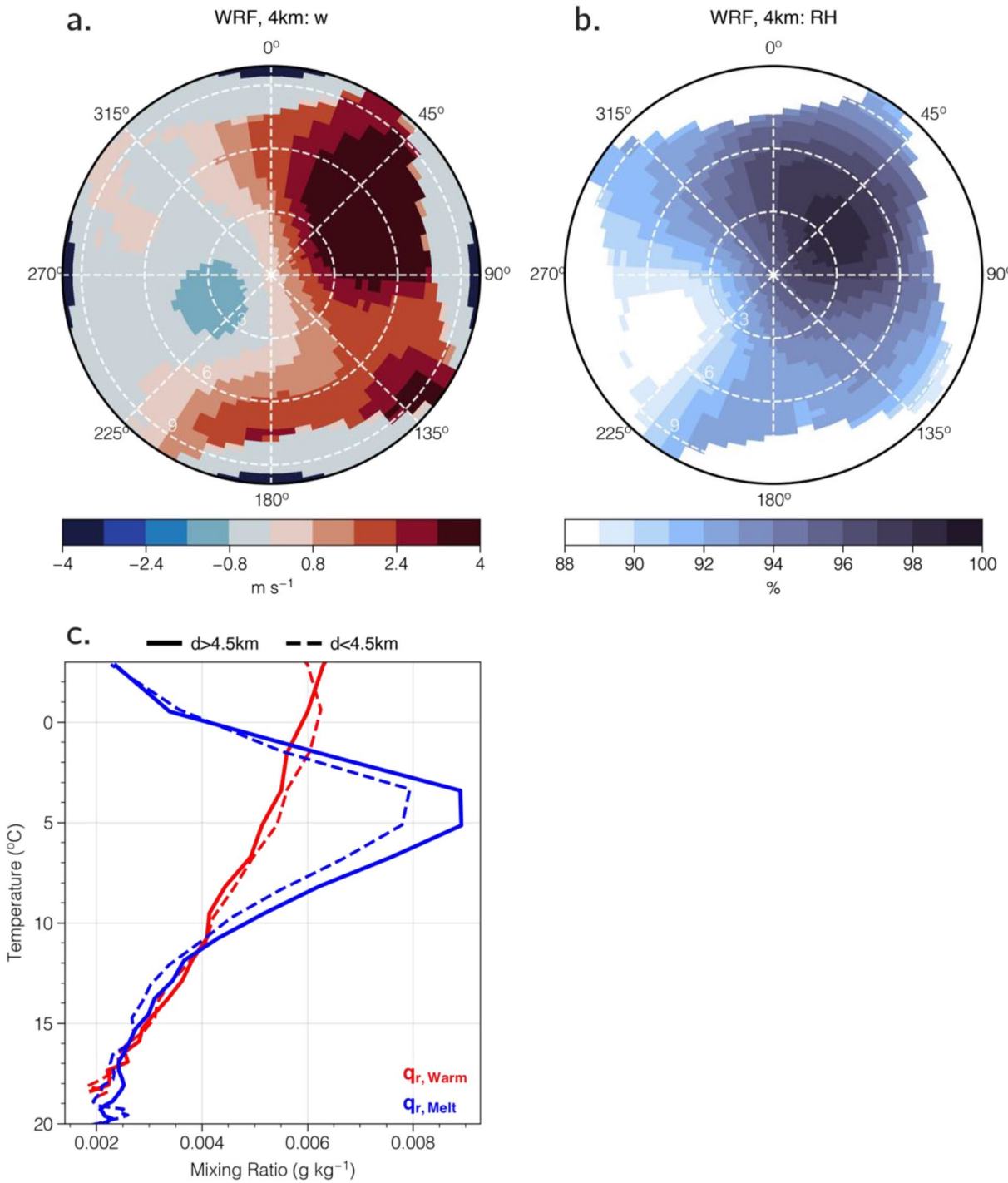

Figure 16. (a)–(b) Similar to Figure 15, but for (a) 4 km vertical velocity, and (b) 4 km relative humidity. (c) Vertical profile of 95th percentile rain mass generated from the cold pathway (solid lines) and the warm pathway (dashed lines) for objects with $d_{WRF} > 4.5$ km (black) and objects with $d_{WRF} < 4.5$ km (red). Celsius temperature is used as the y axis.

When we compare the graupel and rain DSD distributions in polar coordinates, it is clear that the D_{mr} and D_{mg} distributions were rather similar. On the other hand, N_{Tr} distribution maxima were located slightly upwind of the N_{Tg} maxima. Raindrops originated from melted graupel particles further downwind are small and may evaporate before reaching the surface, which could explain the slight spatial displacement between N_{Tr} and N_{Tg} maximum.

In any case, Figure 15 provides the evidence on the role of graupel sedimentation in generating size-sorting signatures. It also suggests that the production and fallout of a small quantity of large graupel particles was critical in spatially separating low-level K_{DP} from Z_{DR}.

6. Discussion

Based on the "particle fountain" model (Yuter & Houze, 1995b; Zeng et al., 2001), we originally hypothesized that areas with larger (smaller) d_{obs} and d_{WRF} at the lower levels would coincide with greater (less) ice DSD spatial separation aloft and stronger (weaker) updrafts. The statistical analyses suggested a more ambiguous relationship between size sorting and convective kinematics than originally hypothesized. While the ETH generally increases with separation distance (d_{obs} and d_{WRF}; Figures 3a, 8a, and 8b), the ETH-separation distances covariance is nonlinear. Thus, it would be difficult to use d_{obs} or d_{WRF} *independently* to diagnose convective kinematics.

The separation distance is shown to be useful in diagnosing other convective properties. Statistical analysis of the PECAN MCSs revealed a clear tendency for more liquid water mass near the melting level for larger d_{obs} objects (Figure 3b). The WRF simulation results support this observational finding by showing more integrated freezing and melting near larger d_{WRF} objects (Figures 10b and 10e). Since the CFAD difference of deposition (Figure 12a) was close to the CFAD difference of freezing (Figure 11a) between –5°C and −25°C, this enhanced freezing likely occurred at the expense of deposition. The CFAD difference also showed more vapor condensation above the melting level for larger d_{WRF} objects than that near smaller d_{WRF} objects (Figure 12b).

Based on these analyses, a microphysical framework was proposed to interpret these findings. For the large d_{WRF} objects.

1. More raindrops and water vapor were lifted to upper levels with subfreezing temperatures. Increased availability of supercooled liquid made it easier for graupel particles to grow by collecting supercooled liquid droplets (riming process; Figures 10b, 11a and 14a)
2. The sedimentation of heavier graupel particles (Figures 14a and 14c) enhanced the cooling by melting (Figures 10e and 11b)

On the other hand, for the smaller d_{WRF} objects.

1. Most raindrops and water vapor stayed at vertical levels with warm temperatures, which reduced freezing heating aloft (Figure 11a)
2. Deposition became the dominant ice generation mechanism in subfreezing temperatures (Figures 10a, 10b and 12a)
3. Ice hydrometeors formed aloft were lighter (Figure 14a) and less likely to fall to warmer temperatures and melt (Figures 11e, 12b and 14c)

These microphysical and thermodynamic processes have important implications on the dominant precipitation pathways associated with different size-sorting object categories. Figure 16c compares the 95-percentile vertical profiles of rain mass generated through the warm pathway (q_{Warm}) and the cold pathway (q_{Melt}) for large and small d_{WRF} objects. Partition of rain mass through the warm and cold pathways follows this equation,

$$\left\{ q_{Warm} = q_{r\_ac} + q_{r\_cn} + q_{r\_cond}, \right. \tag{3a}$$

$$\left\{ q_{Melt} = q_{g\_mlt} + q_{s\_mlt} + q_{i\_mlt}, \right. \tag{3b}$$

where q_{Warm} is the sum of rain mass generated through accretion (q_{r_ac}), autoconversion (q_{r_cn}), and vapor condensation (q_{r_cond}), whereas q_{Melt} is the sum of rain mass generated from melted graupel (q_{g_mlt}), melted snow (q_{s_mlt}), and melted ice (q_{i_mlt}). More q_{Melt} was produced near the large d_{WRF} objects, whereas more q_{Warm} was produced near the small d_{WRF} objects, which agrees with the proposed microphysical framework. The CFAD differences for the graupel number concentration (Figure 14b) and snow concentration (not shown) suggest that the enhanced q_{Melt} was largely related to increased graupel fallout to warmer temperatures. Based on these findings, it was concluded that d_{WRF} could potentially be used to diagnose the amount of rain mass generated via the cold

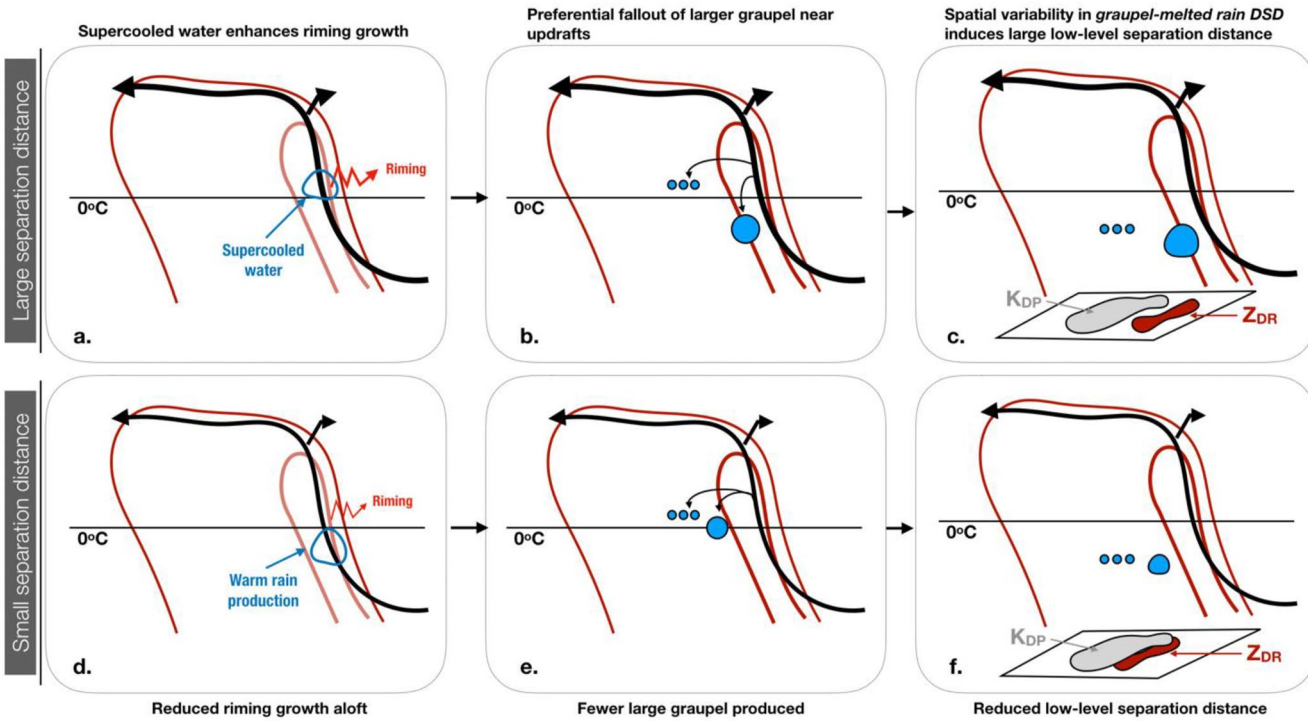

Figure 17. Schematic diagram of the microphysical processes associated with (a–c) larger low-level separation distances, and (d–f) smaller low-level separation distances proposed in Section 6. Black arrows in the diagram represent the system-relative flow pattern. Red contours of line-averaged reflectivity are used to show how the fallout location of graupel (blue circles) differs relative to the mesoscale connective scale.

pathway relative to that generated via the warm pathway. A schematic diagram of the microphysical processes leading to different d_{obs}/d_{WRF} is given in Figure 17.

Finally, the CFAD differences in evaporative and sublimation cooling *magnitudes* between larger d_{WRF} objects and smaller objects (Figures 12c and 12d) indicate a greater likelihood for larger d_{WRF} objects to have stronger evaporative and sublimation cooling at or slightly beneath the melting level. A possible explanation for this is local enhancements in rear inflow jets (RIJs; Yang and Houze, 1995; Grim et al., 2009). Since graupel particles experienced more advection in stronger updrafts, graupel particles formed near large d_{WRF} objects were more likely to sublimate in the drier air behind updrafts (Figure 16b). While there were no in-situ measurements within the convective region of the 20 June MCS, a spiral profile taken in its transition zone did show signs of active sublimation near a strong RIJ (Stechman et al., 2020a; see their Figure 22).

7. Conclusions

This study evaluates the feasibility of using separation distance to infer convective variabilities in nocturnal MCSs during the PECAN field campaign. An object-based method was used to identify a large quantity of size-sorting signatures in the convective regions of 10 nocturnal MCSs. Local kinematic, microphysical, and thermodynamic characteristics were then extracted for each object and compared to its separation distance.

We have listed three scientific questions related to hydrometeor size sorting in the Introduction Section. We now examine if these questions are addressed with the analysis presented. Bivariate statistics show a positive correlation between separation distance and echo-top height (ETH; Figures 3a, 8a, and 8b). Although Figure 13a shows a positive updraft CFAD difference between large d_{WRF} objects and smaller d_{WRF} objects, the statistical difference is mostly statistically insignificant. Thus, we conclude that size-sorting objects' magnitudes could have positive but statistically insignificant correlations to the convective updraft intensities.

Statistically significant differences in thermodynamics and the precipitation pathways were found for objects with different separation distances (d_{WRF}; Figures 10, 11, 12 and 16c). Similarities in the nonlinear correlations between the ETH, IWP, integrated freezing heating and integrated melting cooling (Figures 8b, 8c, 10b and 10e) suggest that changes in convection depth with separation distance can mostly be attributed to the latent heat released through the riming process.

Taking all results presented in Section 5 into account, we find that separation distance can potentially be used to diagnose contributions from riming heating and melting cooling to the overall convective thermodynamic structure (Figures 10b, 10e and 11). Additionally, separation distance may reveal some information about whether convective heating above the melting level is more dominated by deposition or riming (Figures 11a and 12a). More riming growth of graupel particles near large d_{WRF} objects caused the local dominant precipitation pathway to shift more toward the cold pathway (Figure 16c). Statistical analysis of precipitation characteristics (Figures 4 and 9) suggests that increased rain mass generated through the cold pathway near the large d_{WRF} objects contributed to the greater likelihood of intense precipitation. For the smaller d_{WRF} objects, reduced rain production from the cold pathway was partially compensated by warm rain production.

In short, separation distance was shown to be related to different convective variabilities. The most critical factor leading to this correlation is the production and subsequent fallout of large graupel particles. Convective areas would have larger separation distances if there were larger graupel particles in these areas and fell in close vicinity to the updrafts. The correlation between separation distance and graupel growth also indicates that the separation distance can be used to infer the thermodynamic characteristics near and above the melting level.

This study builds upon previous modeling studies that examined different factors leading to the observed polarimetric signatures (e.g., Dawson et al., 2014; Ilotoviz et al., 2018; Kumjian et al., 2014; Snyder et al., 2017). The presented results provided practical guidance on various variabilities near size-sorting signatures of different magnitudes. From a modeling perspective, our results suggest that separation distance can be used to evaluate different microphysical assumptions used in models. For example, the temporal evolution of separation distance can be used to quantify how microphysical assumptions impact the spatial variabilities of drop-size distributions of ice hydrometeors aloft and how these DSD variabilities affect the MCS dynamics.

Finally, while our results are based upon statistical analyses on a large dataset from 10 MCSs during PECAN experiments, uncertainties still remain as to the general applicability of our conclusions, especially for those related to the precipitation pathways. The cold pathway was more important than the warm pathway in generating *intense* precipitation in MCSs during PECAN. However, the warm pathway may be more important in producing rainfall for MCSs occurring in other environments. A climatological analysis of the size-sorting signatures in MCSs over a wide range of geographical locations and seasons is needed to verify our conclusions. We also need to indicate that our results are mostly based on the LLTS 20 June MCS. Discriminating size sorting magnitudes with MCS organizational structure is left to future work. Another limitation of our study is that we have not discussed the interaction between convective drafts and ambient environments. More work is needed to clarify the kinematic variability, possibly through re-classifying size-sorting objects based on updraft width/slope or environmental shear/instability magnitudes. The other limitation is the instantaneous nature of the existing algorithm, which could bias our results against slow-occurring processes. It is also difficult to use the current algorithm to investigate the linkage between separation distances and the life cycle of individual convective elements. Future work should address these limitations by using convection-tracking technique to trace the temporal evolution of different size-sorting objects.

Appendix A

Are the statistical relationships sensitive to model horizontal resolution?

It is possible that the coarser resolution used in this study (a horizontal grid size of 3 km) might not properly represent the size-sorting feature, which is fundamentally a convective-scale process. However, it is evident in Figure A1 that the simulation with a grid size of 3 km can still replicate the *net effect* of the size-sorting phenomenon on spatial distribution and local variability of hydrometeors.

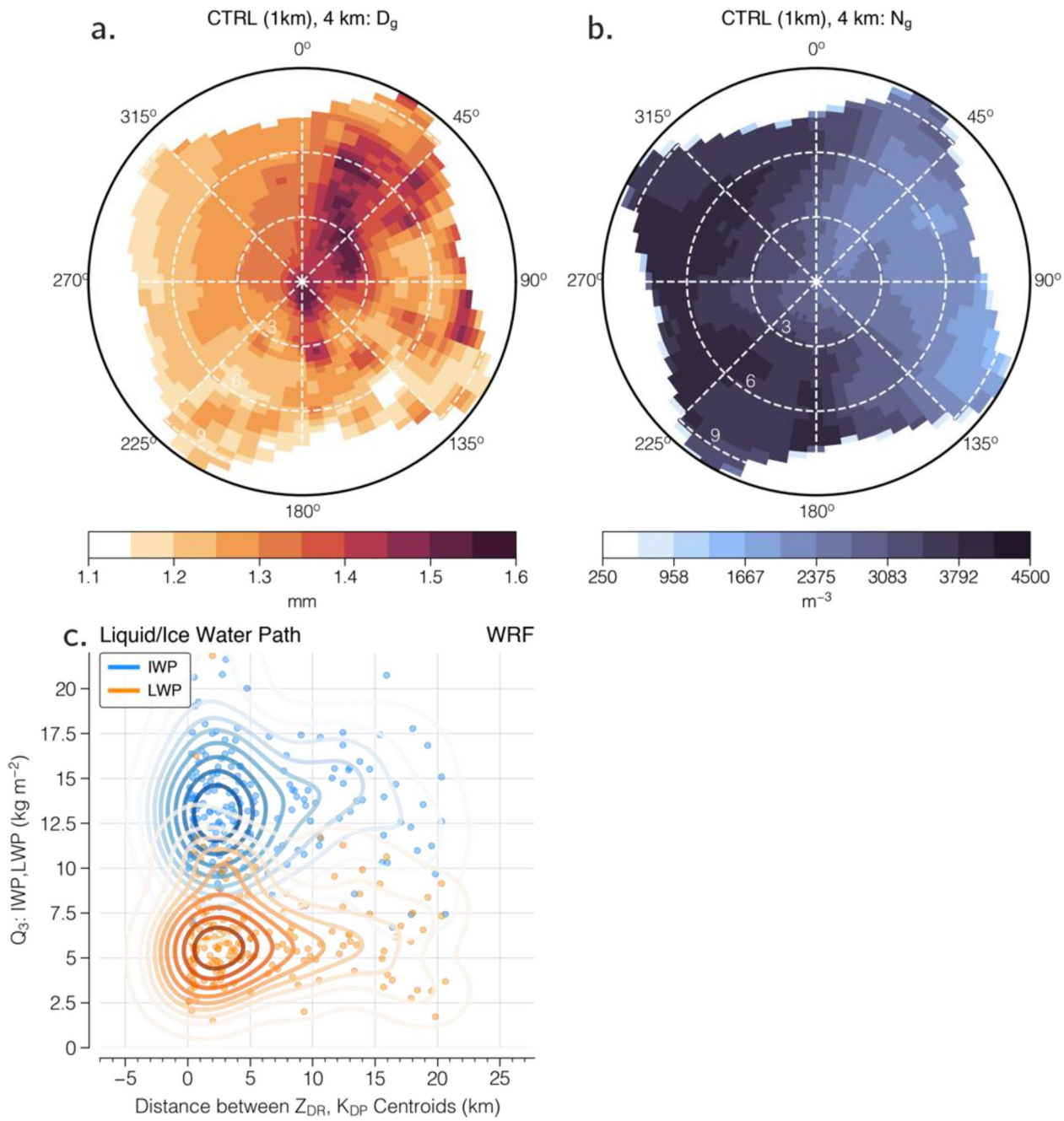

Figure A1. Mean spatial distributions of (a) 4 km graupel diameter, (b) 4 km graupel number concentration surrounding size sorting objects for the simulation with an extra inner domain of 1-km grid spacing. (c) Bivariate scatter plots and normalized frequency distributions between separation distances and (c) liquid and ice water path for the 1-km simulation.

Figure A1 shows the mean spatial distributions of D_{mg} and N_{Tg} at 4-km height from the simulation which has the same model configuration in Table 2 except with 1-km horizontal grid size. Both the coarse and fine grid resolution experiments show a similar spatial trend where D_{mg} (N_{Tg}) concentrates in the upwind or eastern (downwind or western) side of low-level size sorting objects (see Figures 15a, 15b and Figure A1a,A1b). The bivariate distribution between separation distance and ice water path (Figure A1c) continues to increase nonlinearly with d_{WRF} in finer grid resolution. Based on these results, we conclude that even if individual convective drafts could not be well resolved by the simulation with 3-km grid spacing, it still captured *the net effect of several drafts in close proximity*.

Data Availability Statement

The radar observations analyzed in this study can be obtained from the archival website (https://www.ncei.noaa.gov/access/search/data-search/weather-radar-level-ii) hosted by the National Centers for Environmental Information (NCEI) [Data set]. The WRF model is available online at https://github.com/NCAR/WRFV3. [Data set].

Acknowledgments
The authors would like to thank Profs. Ben Jong-Dao Jou and Jen-Ping Chen for their helpful suggestions to this study. Mr. Jyong-En Miao and Mr. Yao-Chu Wu are appreciated for providing support on modeling and data visualization. The authors would like to thank the many PECAN participants for their hard work in obtaining the observational data. The thorough reviews from two anonymous reviewers, whose comments substantially improved the quality of our manuscript, are highly appreciated. This work is supported by the Ministry of Science and Technology of Taiwan under Grant MOST 107-2111-M-002-013 and MOST 108-2111-M-002-011-MY2.

References

Bodine, D. J., & Rasmussen, K. L. (2017). Evolution of mesoscale convective system organizational structure and convective line propagation. *Monthly Weather Review*, *145*(9), 3419–3440. https://doi.org/10.1175/MWR-D-16-0406.1

Braun, S. A., & Houze, R. A., Jr. (1996). The heat budget of a midlatitude squall line and impli-483cations for potential vorticity production. *Journal of the Atmospheric Sciences*, *53*(9), 1217–1240. https://doi.org/10.1175/1520-0469(1996)053<1217:thboam>2.0.co;2

Brown, B. R., Bell, M. M., & Frambach, A. J. (2016). Validation of simulated hurricane drop size distributions using polarimetric radar. *Geophysical Research Letters*, *43*, 910–917. https://doi.org/10.1002/2015GL067278

Cifelli, R., Chandrasekar, V., Lim, S., Kennedy, P. C., Wang, Y., & Rutledge, S. A. (2011). A new dual-polarization radar rainfall algorithm: Application in Colorado precipitation events. *Journal of Atmospheric and Oceanic Technology*, *28*(3), 352–364. https://doi.org/10.1175/2010jtecha1488.1

Cifelli, R., Petersen, W. A., Carey, L. D., Rutledge, S. A., & da Silva Dias, M. A. F. (2002). Radar observations of the kinematic, microphysical, and precipitation characteristics of two MCSs in TRMM-LBA. *Journal of Geophysical Research*, *107*(D20). LBA 44–1–LBA 44–16. https://doi.org/10.1029/2000jd000264

Dawson, D. T., II, Mansell, E. R., Jung, Y., Wicker, L. J., Kumjian, M. R., & Xue, M. (2014). Low-level Zdr signatures in supercell forward flanks: The role of size sorting and melting of hail. *Journal of the Atmospheric Sciences*, *71*(1), 276–299. https://doi.org/10.1175/JAS-D-13-0118.1

Dawson, D. T., II, Xue, M., Milbrandt, J. A., & Yau, M. K. (2010). Comparison of evaporation and cold pool development between single-moment and multimoment bulk microphysics schemes in idealized simulations of tornadic thunderstorms. *Monthly Weather Review*, *138*(4), 1152–1171. https://doi.org/10.1175/2009MWR2956.1

Dawson, D. T., Mansell, E. R., & Kumjian, M. R. (2015). Does wind shear cause hydrometeor size sorting? *Journal of the Atmospheric Sciences*, *72*(1), 340–348. https://doi.org/10.1175/JAS-D-14-0084.1

Didlake, A. C., & Kumjian, M. R. (2018). Examining storm asymmetries in Hurricane Irma (2017) using polarimetric radar observations. *Geophysical Research Letter*, *45*(13), 522. https://doi.org/10.1029/2018GL080739

Dudhia, J. (1989). Numerical study of convection observed during the winter monsoon experiment using a mesoscale two–dimensional model. *Journal of the Atmospheric Sciences*, *46*, 3077–3107. https://doi.org/10.1175/1520-0469(1989)046⟨3077:NSOCOD⟩2.0.CO;2

Feng, Y., & Bell, M. (2018). Microphysical characteristics of an asymmetric eyewall in major hurricane Harvey. *Geophysical Research Letter*, *46*, 461–471. https://doi.org/10.1029/2018GL080770

Gabella, M., & Notarpietro, R. (2002). *Ground Clutter Characterization and Elimination in Mountainous Terrain* (pp. 305–311).

Gallus, W. A., Jr., & Johnson, R. H. (1991). Heat and moisture budgets of an intense midlatitude squall line. *Journal of the Atmospheric Sciences*, *48*(1), 122–146. https://doi.org/10.1175/1520-0469(1991)048<0122:hamboa>2.0.co;2

Geerts, B., Parsons, D., Ziegler, C. L., Weckwerth, T. M., Biggerstaff, M. I., Clark, R. D., et al. (2017). The 2015 plains elevated convection at night field project. *Bulletin of the American Meteorological Society*, *98*(4), 767–786. https://doi.org/10.1175/BAMS-D-15-00257.1

Grim, J. A., Rauber, R. M., McFarquhar, G. M., Jewett, B. F., & Jorgensen, D. P. (2009). Development and forcing of the rear inflow jet in a rapidly developing and decaying squall line during BAMEX. *Monthly Weather Review*, *137*(4), 1206–1229. https://doi.org/10.1175/2008MWR2503.1

Helmus, J., & Collis, S. (2016). The Python ARM Radar Toolkit (Py-ART), a library for working with weather radar data in the Python programming language. *Journal of Open Research Software*, *5114*(1), e25. https://doi.org/10.5334/jors.119

Homeyer, C. R., & Kumjian, M. R. (2014). Microphysical characteristics of overshooting convection from polarimetric radar observations. *Journal of the Atmospheric Sciences*, *72*(2), 870–891. https://doi.org/10.1175/JAS-D-13-0388.1

Houze, R. A. Jr., Biggerstaff, M. I., Rutledge, S. A., & Smull, B. F. (1989). Interpretation of Doppler weather radar displays of mid-latitude mesoscale convective systems. *Bulletin of the American Meteorological Society*, *70*(9), 608–619. https://doi.org/10.1175/1520-0477(1989)070<0608:iodwrd>2.0.co;2

Ilotoviz, E., Khain, A., Ryzhkov, A. V., & Snyder, J. C. (2018). Relationship between aerosols, hail microphysics, and ZDR columns. *Journal of the Atmospheric Sciences*, *75*(6), 1755–1781. https://doi.org/10.1175/JAS-D-17-0127.1

Janjic, Z. I. (1994). The step-mountain eta coordinate model: Further developments of the convection, viscous sublayer, and turbulence closure schemes. *Monthly Weather Review*, *122*(5), 927–945. https://doi.org/10.1175/1520-0493(1994)122⟨0927:TSMECM⟩2.0.CO;2

Jensen, A. A., Harrington, J. Y., & Morrison, H. (2018). Microphysical characteristics of squall-line stratiform precipitation and transition zones simulated using an ice particle property-evolving model. *Monthly Weather Review*, *146*(3), 723–743. https://doi.org/10.1175/MWR-D-17-0215.1

Jung, Y., Xue, M., & Zhang, G. (2010). Simulations of polarimetric radar signatures of a supercell storm using a two-moment bulk microphysics scheme. *Journal of Applied Meteorology and Climatology*, *49*(1), 146–163. https://doi.org/10.1175/2009JAMC2178.1

Kain, J. S. (2004). The Kain–Fritsch convective parameterization: An update. *Journal of Applied Meteorology*, *43*(1), 170–181.

Kain, J. S., Goss, S. M., & Baldwin, M. E. (2000). The melting effect as a factor in precipitation-type forecasting. *Weather and Forecasting*, *15*(6), 700–714. https://doi.org/10.1175/1520-0434(2000)015⟨0700:TMEAAF⟩2.0.CO;2

Kolmogorov, A. (1933). Sulla determinazione empirica di una legge di distributione. *Giornale dell'Istituto Italiano degli Attuari*, *4*, 1–11.

Kumjian, M. R., Khain, A. P., Benmoshe, N., Ilotoviz, E., Ryzhkov, A. V., & Phillips, V. T. J, (2014). The anatomy and physics of Zdr columns: Investigating a polarimetric radar signature with a spectral bin microphysical model. *Journal of Applied Meteorology and Climatology*, *53*(7), 1820–1843. https://doi.org/10.1175/JAMC-D-13-0354.1

Kumjian, M. R., & Prat, O. P. (2014). The impact of raindrop collisional processes on the polarimetric radar variables. *Journal of the Atmospheric Sciences*, *71*(8), 3052–3067. https://doi.org/10.1175/JAS-D-13-0357.1

Kumjian, M. R., & Ryzhkov, A. V. (2008). Polarimetric signatures in supercell thunderstorms. *Journal of Applied Meteorology and Climatology*, *47*(7), 1940–1961. https://doi.org/10.1175/2007JAMC1874.1

Kumjian, M. R., & Ryzhkov, A. V. (2012). The impact of size sorting on the polarimetric radar variables. *Journal of the Atmospheric Sciences*, *69*(6), 2042–2060. https://doi.org/10.1175/JAS-D-11-0125.1

Lang, T. J., Ahijevych, D. A., Nesbitt, S. W., Carbone, R. E., Rutledge, S. A., & Cifelli, R. (2007). Radar-observed characteristics of precipitating systems during NAME 2004. *Journal of Climate*, *20*(9), 1713–1733. https://doi.org/10.1175/JCLI4082.1

Lasher-Trapp, S., Kumar, S., Moser, D. H., Blyth, A. M., French, J. R., Jackson, R. C., et al. (2018). On different microphysical pathways to convective rainfall. *Journal of Applied Meteorology and Climatology*, *57*(10), 2399–2417. https://doi.org/10.1175/JAMC-D-18-0041.1

Laurencin, C. N., Didlake, A. C., Loeffler, S. D., Kumjian, M. R., & Heymsfield, G. M. (2020). Hydrometeor size sorting in the asymmetric eyewall of Hurricane Matthew (2016). *Journal of Geophysical Research*, *125*, e2020JD032671. https://doi.org/10.1029/2020JD032671

Loeffler, S. D., & Kumjian, M. R. (2018). Quantifying the separation of enhanced Zdr and Kdp regions in nonsupercell tornadic storms. *Weather and Forecasting*, *33*(5), 1143–1157. https://doi.org/10.1175/WAF-D-18-0011.1

Loeffler, S. D., Kumjian, M. R., Jurewicz, M., & French, M. M. (2020). Differentiating between tornadic and nontornadic supercells using polarimetric radar signatures of hydrometeor size sorting. *Geophysical Research Letter*, *47*(12). e2020GL088242. https://doi.org/10.1029/2020GL088242

Mansell, E. R., Ziegler, C. L., & Bruning, E. C. (2010). Simulated electrification of a small thunderstorm with two-moment bulk microphysics. *Journal of the Atmospheric Sciences*, *67*(1), 171–194. https://doi.org/10.1175/2009JAS2965.1

Marinescu, P. J., vanden Heever, S. C., Saleeby, S. M., & Kreidenweis, S. M. (2016). The microphysical contributions to and evolution of latent heating profiles in two MC3E MCSs. *Journal of Geophysical Research*, *121*, 7913–7935. https://doi.org/10.1002/2016JD024762

Martinaitis, S. M. (2017). Radar observations of tornado-warned convection associated with tropical cyclones over Florida. *Weather and Forecasting*, *32*(1), 165–186. https://doi.org/10.1175/WAF-D-16-0105.1

Massey, F. J., Jr. (1951). The Kolmogorov-Smirnov test for goodness of fit. *Journal of the American Statistical Association*, *46*(253), 68–78. https://doi.org/10.1080/01621459.1951.10500769

Mesinger, F., DiMego, G., Kalnay, E., Mitchell, K., Shafran, P. C., Ebisuzaki, W., et al. (2006). North American regional Reanalysis. *Bulletin of the American Meteorological Society*, *87*(3), 343–360. https://doi.org/10.1175/BAMS-87-3-343

Mlawer, E. J., Taubman, S. J., Brown, P. D., Iacono, M. J., & Clough, S. A. (1997). Radiative transfer for inhomogeneous atmospheres: RRTM, a validated correlated-k model for the longwave. *Journal of Geophysical Research*, *102*(D14), 16663–16682. https://doi.org/10.1029/97JD00237

Morrison, H. (2016). Impacts of updraft size and dimensionality on the perturbation pressure and vertical velocity in cumulus convection. Part II: Comparison of theoretical and numerical solutions and fully dynamical simulations. *Journal of the Atmospheric Sciences*, *73*(4), 1455–1480. https://doi.org/10.1175/JAS-D-15-0041.1

Morrison, H., Tessendorf, S. A., Ikeda, K., & Thompson, G. (2012). Sensitivity of a simulated midlatitude squall line to parameterization of raindrop breakup. *Monthly Weather Review*, *140*(8), 2437–2460. https://doi.org/10.1175/MWR-D-11-00283.1

Parker, M. D., & Johnson, R. H. (2000). Organizational modes of midlatitude mesoscale convective systems. *Monthly Weather Review*, *128*, 3413–3436. https://doi.org/10.1175/1520-0493(2001)129⟨3413:OMOMMC⟩2.0.CO;2

Parker, M. D. (2010). Relationship between system slope and updraft intensity in squall lines. *Monthly Weather Review*, *138*(9), 3572–3578. https://doi.org/10.1175/2010MWR3441.1

Peters, J. M. (2016). The impact of effective buoyancy and dynamic pressure forcing on vertical velocities within two-dimensional updrafts. *Journal of the Atmospheric Sciences*, *73*(11), 4531–4551. https://doi.org/10.1175/JAS-D-16-0016.1

Planche, C., Tridon, F., Banson, S., Thompson, G., Monier, M., Battaglia, A., & Wobrock, W. (2019). On the realism of the rain microphysics representation of a squall line in the WRF model. Part II: Sensitivity studies on the rain drop size distributions. *Monthly Weather Review*, *147*(8), 2811–2825. https://doi.org/10.1175/MWR-D-18-0019.1

Rauber, R. M., & Nesbitt, S. W. (2018). *Radar Meteorology: A first Course* (p. 488). Wiley-Blackwell.

Ryzhkov, A. V., & Zrnic, D. S. (1998). Discrimination between rain and snow with a polarimetric radar. *Journal of Applied Meteorology*, *37*(10), 1228–1240. https://doi.org/10.1175/1520-0450(1998)037⟨1228:DBRASW⟩2.0.CO;2

Skamarock, W., Klemp, J., Dudhia, J., Gill, D., Barker, D., Wang, W., & Powers, J. (2008). *A description of the advanced research WRF, version 3.27, 3–27* (p. 113). NCAR Tech. Note NCAR/TN-4751STR.

Smirnov, H. (1939). Sur les écarts de la courbe de distribution empirique. *Recueil Mathématique (Matemnticeskii Sbornik), N.S.*, *6*, 3–26.

Snyder, J. C., Bluestein, H. B., Dawson, D. T., II, & Jung, Y. (2017). Simulations of polarimetric, X-band radar signatures in supercells. Part II: Zdr columns and rings and Kdp columns. *Journal of Applied Meteorology and Climatology*, *56*(7), 2001–2026. https://doi.org/10.1175/JAMC-D-16-0139.1

Stanford, M. W., Varble, A., Zipser, E., Strapp, J. W., Leroy, D., Schwarzenboeck, A., et al. (2017). A ubiquitous ice size bias in simulations of tropical deep convection. *Atmospheric Chemistry and Physics*, *17*(15), 9599–9621. https://doi.org/10.5194/acp-17-9599-2017

Stechman, D. M., McFarquhar, G. M., Rauber, R. M., Bell, M. M., Jewett, B. F., & Martinez, J. (2020). Spatiotemporal evolution of the microphysical and thermodynamic characteristics of the 20 June 2015 PECAN MCS. *Monthly Weather Review*, *148*(4), 1363–1388. https://doi.org/10.1175/mwr-d-19-0293.1

Stechman, D. M., McFarquhar, G. M., Rauber, R. M., Jewett, B. F., & Black, R. A. (2020). Composite in situ microphysical analysis of all spiral vertical profiles executed within BAMEX and PECAN mesoscale convective systems. *Journal of the Atmospheric Sciences*, *77*(7), 2541–2565. https://doi.org/10.1175/JAS-D-19-0317.1

Steiner, M., Houze, R. A., Jr., & Yuter, S. E. (1995). Climatological characterization of three-dimensional storm structure from operational radar and rain gauge data. *Journal of Applied Meteorology and Climatology*, *34*(9), 1978–2007. https://doi.org/10.1175/1520-0450(1995)034⟨1978:CCOTDS⟩2.0.CO;2

Storer, R. L., & van den Heever, S. C. (2013). Microphysical processes evident in aerosol forcing of tropical deep convective clouds. *Journal of the Atmospheric Sciences*, *70*(2), 430–446. https://doi.org/10.1175/JAS-D-12-076.1

Tao, W.-K., Scala, J., Ferrier, B., & Simpson, J. (1995). The effects of melting processes on the development of a tropical and a midlatitude squall line. *Journal of Atmospheric Sciences*, *52*(11), 1934–1948. https://doi.org/10.1175/1520-0469(1995)052⟨1934:TEOMPO⟩2.0.CO;2

Tewari, M., Chen, F., Wang, W., Dudhia, J., LeMone, M. A., Mitchell, K., et al. (2004). Implementation and verification of the unified NOAH land surface model in the WRF model. *20th Conference on weather analysis and Forecasting/16th Conference on numerical weather prediction*, (pp. 11–15).

Varble, A., Fridlind, A. M., Zipser, E. J., Ackerman, A. S., Chaboureau, J.-P., Fan, J., et al. (2011). Evaluation of cloud-resolving model intercomparison simulations using two-ice observations: Precipitation and cloud structure. *Journal of Geophysical Research*, *116*(D12206). https://doi.org/10.1029/2010JD015180

Varble, A., Zipser, E. J., Fridlind, A. M., Zhu, P., Ackerman, A. S., Chaboureau, J.-P., et al. (2014). Evaluation of cloud-resolving and limited area model intercomparison simulations using two-ice observations: 1. Deep convective updraft properties. *Journal of Geophysical Research: Atmospheres*, *119*(24), 13891–13913. https://doi.org/10.1002/2013JD021371

Wu, D., Dong, X., Xi, B., Feng, Z., Kennedy, A., Mullendore, G., et al. (2013). Impacts of microphysical scheme on convective and stratiform characteristics in two high precipitation squall line events. *Journal of Geophysical Research: Atmospheres*, *118*, 11119–11211. https://doi.org/10.1002/jgrd.50798

Yang, M.-J., & Houze, R. A., Jr. (1995). Sensitivity of squall-line rear inflow to ice microphysics and environmental humidity. *Monthly Weather Review*, *123* (11), 3175–3193. https://doi.org/10.1175/1520-0493(1995)123<3175:soslri>2.0.co;2

Yuter, S. E., & Houze, R. A., Jr. (1995a). Three-dimensional kinematic and microphysical evolution of Florida cumulonimbus. Part II: Frequency distributions of vertical velocity, reflectivity, and differential reflectivity. *Monthly Weather Review*, *123* (7), 1941–1963. https://doi.org/10.1175/1520-0493(1995)123<1941:tdkame>2.0.co;2

Yuter, S. E., & Houze, R. A., Jr. (1995b). Three-dimensional kinematic and microphysical evolution of Florida cumulonimbus. Part III: Vertical mass transport, mass divergence, and synthesis. *Monthly Weather Review*, *123* (7), 1964–1983. https://doi.org/10.1175/1520-0493(1995)123<1964:tdkame>2.0.co;2

Zeng, Z., Yuter, S. E., Houze, R. A., Jr., & Kingsmill, D. E. (2001). Microphysics of the rapid development of heavy convective precipitation. *Monthly Weather Review*, *129*(8), 1882–1904. https://doi.org/10.1175/1520-0493(2001)129⟨1882:MOTRDO⟩2.0.CO;2

Zittel, W. D., Cunningham, J. G., Lee, R. R., Richardson, L. M., Ice, R. L., & Melnikov, V. (2014). Use of hydrometeors, Bragg scatter, and sun spikes to determine system ZDR biases in the WSR-88D fleet. Extended Abstracts, Eighth European Conf. On radar in Meteorology and Hydrology (ERAD 2014), Garmisch-Partenkirchen, Germany, DWD and DLR, DAC.P12. Retrieved from https://www.roc.noaa.gov/WSR88D/PublicDocs/Publications/132_Zittel.pdf